



UNIVERSITÀ DEGLI STUDI DI NAPOLI FEDERICO II

**DOTTORATO DI RICERCA IN INGEGNERIA AEROSPAZIALE, NAVALE E DELLA QUALITÀ
SCUOLA DI DOTTORATO DI RICERCA IN INGEGNERIA INDUSTRIALE
INDIRIZZO: INGEGNERIA AEROSPAZIALE
XXII CICLO**

ALTIMETRY BY CASSINI RADAR: PROCESSING AND SIMULATION

Coordinatore: Ch.mo Prof A. Moccia

Dottorando: Giovanni Alberti

A Maria Grazia che voleva sposare un Dottore

**ALTIMETRY BY CASSINI RADAR:
PROCESSING AND SIMULATION**

Giovanni Alberti

Novembre 2009

TABLE OF CONTENT

1	INTRODUCTION	16
2	SATELLITE ALTIMETRY	18
3	THE CASSINI MISSION TO TITAN.....	26
4	WAVEFORM MODEL DEVELOPMENT	28
5	MODELS ERROR BUDGET	37
6	HEIGHT RETRIEVAL ALGORITHM	43
7	ALGORITHM CORRECTION.....	56
8	PAD SYSTEM	60
9	PROCESSING RESULTS.....	70
10	SIMULATION.....	76
11	CONCLUSIONS.....	92
12	APPENDIX A – NADIR MODEL	94

LIST OF FIGURES

Figure 1 – Geometry of a nadir oriented (a) beamwidth-limited altimeter (dP>dB) and (b) pulsewidth-limited altimeter (dP<dB)	24
Figure 2 – Conventional Pulse Limited illumination geometry	25
Figure 3 – Off-nadir altimetry geometry	33
Figure 4 - Theoretical impulse response (H=5000 Km, $\xi=0.15^\circ$) for various surface height r.m.s. values ($\sigma_h=10m; 50m; 100m$)	39
Figure 5 - Relative errors for all models (H=5000 Km, $\xi=0.15^\circ$).....	40
Figure 6 - Mean integral relative error for all models as a function of spacecraft altitude ($\xi=0.15^\circ$).....	41
Figure 7 - Mean integral relative error for all models as a function of off-nadir angle (H=6000 Km).....	42
Figure 8 - Algorithm for actual implementation of MLE method.....	49
Figure 9 - Impulse response time width (second central moment) as a function of off-nadir angle for various spacecraft altitude (H) values (4000 Km up to 9000 Km, step 1000 Km). The values have been evaluated on the basis of developed analytical models and they are used for correcting the off-nadir angle to be used for the MLE procedure.	50
Figure 10 - Simulated Cassini radar echoes with H=5000 Km and $\xi=0.15^\circ$ - some realizations (top) and the averaged echo (bottom)	51
Figure 11 - Height error: statistical results obtained by applying the MLE algorithm (1000 simulations) as a function of off-nadir angle for various spacecraft altitude (4000 km up to 9000 km with 1000 km step) – mean (top) and standard deviation (bottom) values.	52
Figure 12 - Normalized sigma nought error: statistical results obtained by applying the MLE algorithm (1000 simulations) as a function of off-nadir angle for various spacecraft altitude(4000 km up to 9000 km, 1000 km step) - mean (top) and standard deviation (bottom) values.	53
Figure 13 - Delay between waveform centroid and true height evaluated on the basis of developed analytical models, as a function of off-nadir angle and for various spacecraft altitude (H) values (4000 Km up to 9000 Km, step 1000 Km). The corresponding time delay is used for initializing MLE algorithm.	54
Figure 14 - Model amplitude values for getting a resulting normalized model, as a function of off-nadir angle and for various spacecraft altitude (H) values (4000 Km up to 9000 Km, step 1000 Km).....	55

Figure 15 – Altimeter impulse response evaluated by using near-nadir model for various off-nadir angle values	58
Figure 16 – Model’s integral (I) as a function of the off-nadir angle for various radar altitude (H ranging from 6 Km to 12 Km, 1 Km step).....	58
Figure 17 – Model’s standard variation (σ) as a function of the off-nadir angle for various radar altitude (H ranging from 6 Km to 12 Km, 1 Km step).....	59
Figure 18 - PAD System Physical Architecture	61
Figure 19 - PAD Tools Architectural Design.....	67
Figure 20 – The PAD Framework	68
Figure 21 – The Production Tool HMI.....	68
Figure 22 – The Science Look Tool HMI	69
Figure 23 – The Map Tool HMI.....	69
Figure 24 - Retrieved Titan’s surface height as a function of along track distance. The height values are referred to Titan’s mean radius of 2575 Km (fly-bys T13, T16 and T19). The distance values are referred to altimetric acquisition start.	71
Figure 25 - Retrieved Titan’s surface height as a function of along track distance. The height values are referred to Titan’s mean radius of 2575 Km (fly-bys T21, T23 and T25). The distance values are referred to altimetric acquisition start.	72
Figure 26 - Retrieved Titan’s surface height as a function of along track distance. The height values are referred to Titan’s mean radius of 2575 Km (fly-bys T28, T29 and T3). The distance values are referred to altimetric acquisition start.	73
Figure 27 - Retrieved Titan’s surface height as a function of along track distance. The height values are referred to Titan’s mean radius of 2575 Km (fly-bys T30, T8 and Ta). The distance values are referred to altimetric acquisition start.	74
Figure 28 – Fractal surface generated with $H=0.65$ and $T=0.005$. All negative values have been set to zero for simulating presence of liquid materials.....	78
Figure 29 – Backscattering coefficient for CASSINI radar as a function of the incidence angle for various H values (H from 0.6 to 0.85, step 0.05)	81
Figure 30 – Backscattering coefficient for CASSINI radar as a function of the incidence angle for various T values.....	81
Figure 31 – Algorithm used for simulating CASSINI radar received power echoes.....	83
Figure 32 – Examples of simulated CASSINI radar waveforms and the resulting averaging.....	84

Figure 33 – Simulated waveform: I moment as a function of Topothesy for various radar altitude, Hurst coefficient and off-nadir angle values.....	86
Figure 34 – Simulated waveform: II moment as a function of Topothesy (upper figure) and off-nadir angle (lower figure) for various radar altitude, Hurst coefficient and off-nadir angle values.....	87
Figure 35 – Simulated waveform: skewness moment as a function of Topothesy (lower figure) and off-nadir angle (upper figure) for various radar altitude, Hurst coefficient and off-nadir angle values.....	88
Figure 36 – Radargram of T30 fly-by: the two dotted red lined limit the zone where the procedure for estimating the fractal parameters of the surface has been applied	89
Figure 37 – Results of the procedure for estimating the fractal parameters applied to T30 fly-by	90
Figure 38 – Final results of the procedure for estimating the fractal parameters applied to T30 fly-by	91
Figure 39 – Geometry for flat-surface impulse response evaluation	96

LIST OF TABLES

Table 1 – Main parameter for the HI-RES CASSINI altimeter	27
Table 2- Exponential and amplitude factors for Prony’s approximation	35
Table 3 – Mean integral relative error for all models.....	39
Table 4 – Threshold values for off-nadir angle and corresponding model for assuring a MIRE less than 1 %	42
Table 5 - Main statistical information of the 11 fly-bys with available high resolution altimetric data. The slope values are evaluated separately for in-bound (in) and out-bound (out) part of the trajectory.	75

ABBREVIATION

ABDR	Altimeter Burst Data Record
AHAG	Cassini ALTH with Auto Gain
ALAG	Cassini ALTL with Auto Gain
ALT	Cassini Radar Altimeter
ALTH	Cassini Altimeter High-Resolution
ALTL	Cassini Altimeter Low-Resolution
ASDC	ASI Science Data Center
ASI	Agenzia Spaziale Italiana
BL	Beam Limited
BODP	Burst Ordered Data Products
COTS	Commercial Off The Shelf
DAS	Data Archiving Subsystem
ESA	European Space Agency
FSIR	Flat Surface Impulse Response
FTP	File transfer Protocol
GUI	Graphical User Interface
HW	Hardware
IR	Impulse Response
ISS	Imaging Science Subsystem
JPL	Jet Propulsion Laboratory
LBDR	Long Burst Data Record
MLE	Maximum Likelihood Estimator
MT	Map Tool
PAD	Processing of Altimeter Data
PDS	Planetary Data System
PL	Pulse Limited

PT	Production Tool
RA	Radar Altimeter
SBDR	Short Burst Data Record
S/C	Spacecraft
SDE	Software Development Environment
SIS	Software Interface Specification
SLT	Science Look Tool
SUM	SW User Manual
SW	Software
TBF	Target Body Fixed

REFERENCES

- [1] C. Elachi, M. D. Allison, L. Borgarelli, P. Encrenaz, E. Im, M. A. Janssen, W. T. K. Johnson, R. L. Kirk, R. D. Lorenz, J. I. Lunine, D. O. Muhleman, S. J. Ostro, G. Picardi, F. Posa, C. G. Rapley, L. E. Roth, R. Seu, L. A. Soderblom, S. Vetrella, S. D. Wall, C. A. Wood and H. A. Zebker, “The Cassini Radar Titan Mapper”, *Space Science Reviews*, 1–40, 2004 Kluwer Academic Publishers
- [2] C. Elachi, E. Im, L.E. Roth, C.L. Werner, “Cassini Titan Radar Mapper”, *Proceedings of the IEEE*, Volume 79, Issue 6, June 1991 pp. 867–880
- [3] G. Franceschetti, P. S. Callahan, A. Iodice, D. Riccio, S. D. Wall, “Titan, Fractals, and Filtering of Cassini Altimeter Data”, *IEEE Transactions on Geoscience and Remote Sensing*, Vol. 44, no. 8, August 2006
- [4] Abramowitz, M., Stegun, I.A., Eds., ”Handbook of Mathematical Functions”, *Dover Publications*, New York 1972
- [5] G. Franceschetti, A. Iodice, M. Migliaccio, D. Riccio, “Scattering from Natural Rough Surfaces Modeled by Fractional Brownian Motion Two-Dimensional Processes”, *IEEE Transactions on Antennas and Propagation*, vol. 47, no. 9, September 1999
- [6] Borgarelli, L., G. Picardi, R. Seu, and E. Zampolini Faustini, “Altimetry in the Cassini mission”, *IGARSS’95*, Florence, 1995, pp.1598-1600
- [7] Brown, G.S., “A useful approximation for the flat surface impulse response”, *Antennas and Propagation*, *IEEE Transactions on*, Vol. 37, Issue 6, Jun. 1989, pp. 764-767
- [8] Brown, G.S., “The average impulse response of a rough surface and its applications”, *IEEE Transactions on Antennas and Propagation*, Vol. 25, Issue 1, Jan. 1977, pp. 67-74
- [9] CAS-3-170, “Cassini Orbiter Functional Requirements Book, Accuracy Requirements and System Capabilities, Rev. D”, November 7, 1997, *Jet Propulsion Laboratory*
- [10] Davis, C.H., “Satellite radar altimetry”, *IEEE Transactions on Microwave Theory and Techniques - Special Issue: Microwaves in Space*, Vol. 40, No. 6, Jun. 1992, pp. 1070-1076
- [11] Hildebrand, F. B., “Introduction to Numerical Analysis”, *New York: McGraw-Hill*, 1956, pp. 378-382
- [12] Lunine, J. I.; Soderblom, L A., “Cassini-Huygens investigations of satellite surfaces and interiors”, *Space Science Reviews*, Vol. 104, no. 1-4, pp. 191-208. 2002

- [13] Montefredini, E., Morelli, F., Picardi, G., Seu, R., “A non-coherent surface backscattering model for radar observation of planetary bodies and its application to Cassini Radar altimeter”, *Planetary Space Science*, Vol. 43, No. 12, 1995, pp. 1567-1577
- [14] Moore, R.K., Williams, C.S., “Radar terrain return at near-vertical incidence”, *Proc. IRE.*, 45, 1957, pp. 228–238
- [15] Muhleman, D.O.; Grossman, A.W.; Butler, B.J.; Slade, M.A., “Radar reflectivity of Titan”, *Science* (ISSN 0036-8075), vol. 248, May 25, 1990, p. 975-980
- [16] Newkirk, M.H., Brown, G.S, “Issues related to waveform computations for radar altimeter applications”, *IEEE Transactions on Antennas and Propagation*, Vol. 40, Issue 12, Dec. 1992, pp. 1478-1488
- [17] Bender, C.M., Orzag, S.A., “Advanced Mathematical Methods for Scientists and Engineers”, *New York: McGraw-Hill*, 1978
- [18] A. Van Trees, “Detection estimation and modulation theory” (part I), *John Wiley*, 1968
- [19] B. B. Mandelbrot, *The Fractal Geometry of Nature*. New York: Freeman, 1983.
- [20] J. S. Feder, *Fractals*. New York: Plenum, 1988.
- [21] S. R. Brown and C. H. Sholz, “Broad band study of the topography of natural rock surfaces,” *J. Geophys. Res.*, vol. 90, pp. 12575–12 582, Dec. 1985.
- [22] B. B. Mandelbrot and V. Ness, “Fractional Brownian motions, fractional noises and applications,” *SIAM Rev.*, vol. 10, pp. 422–437, Oct. 1968.
- [23] P. Flandrin, “On the spectrum of fractional brownian motions,” *IEEE Trans. Inf. Theory*, vol. 35, no. 1, pp. 197–199, 1989.
- [24] G. W. Wornell, *Signal Processing With Fractals*. Upper Saddle River, NJ: Prentice-Hall, 1996.
- [25] G. Franceschetti, A. Iodice, M. Migliaccio, and D. Riccio, “Scattering from natural rough surfaces modeled by fractional brownian motion two-dimensional processes,” *IEEE Trans. Antennas Propag.*, vol. 47, no. 9, pp. 1405–1415, Oct. 1999.

ACKNOWLEDGMENT

The research consortium CO.R.I.S.T.A. at Naples and the Italian Space Agency (ASI) that mainly funded these activities, are gratefully acknowledged for supplying me with the opportunity to work in the frame of Cassini Mission.

I would like to thank all my colleagues involved in the Cassini mission for their fruitful collaboration and suggestions. During last years, I was participating to the Cassini Altimetry Working Group that has made great efforts for the assessment of processing algorithms for the retrieval of Titan's surface height. This team has been initiated by a joint agreements between ASI and NASA and it has been coordinated by Enrico Flamini and Steve Wall.

I would like to thank all people involved in this group especially Roberto Seu, Roberto Orosei, Phil Callahan, Howard Zebker, William T. K. Johnson and Yonggyu Gim.

ABSTRACT

The Cassini mission, that is a joint NASA/ESA/ASI effort, has recently offered the unique possibility of exploring Titan, the largest moon of Saturn, that is the only satellite in the solar system to host an appreciable atmosphere, which unfortunately made the surface below very difficult to be observed from the Earth with optical instruments. In fact, a smoggy haze, mostly composed of aerosols resulting from photochemistry between methane and hydrogen and other hydrocarbons, completely envelops the satellite.

The Radar Altimeter of the Cassini Mission to Titan operates in a transition region between pulse and beam-limited condition. Due to the specific observation geometry, low values of mispointing angle have been found to significantly affect altimeter impulse response. This involves a non-conventional formulation of the system response which has been the main goal of this research doctorate.

An analytical model of the average return power waveform, valid for near-nadir altimetry measurements, has been developed in order to cope with the particular operating conditions of Cassini Mission. The model used to approximate the altimeter waveform is based on the same general assumptions of the classical Brown's model (1977), but exploits a flat surface response approximation by Prony's methods. Both theoretical considerations and simulated data have been taken into account to support the accuracy of the proposed model.

To infer the main geophysical parameters describing surface topography from altimetry data, a parametric estimation procedure has been used. The Maximum Likelihood Estimator (MLE) procedure has been chosen since in principle it can assure optimal performance as consequence of the analytical model we used to describe the system impulse response.

Performances of the implemented method have been numerically evaluated through simulation of data received by CASSINI in high-resolution altimeter mode.

The algorithms have been implemented in specific software tools for processing, managing, visualizing and archiving scientific output products containing all the retrieved information about the Titan surface topography, starting from the raw data as delivered by JPL/NASA. The developed processing system is currently in charge of producing standard altimetric Cassini products to be archived in the Planetary Data System (PDS) format. The retrieved topography of the fly-bys performed up to now are shown and shortly commented.

Further activities have been dedicated to altimetry echo waveform simulation. The main reason for this effort is to better understand the Titan's surface characteristics by analyzing the signals received by CASSINI radar in altimetric mode.

The approach followed is based on a fractal characterization of Titan's surface that enables a closed form for the scattering coefficient.

A preliminary analysis has been performed on actual data (T30 fly-by) for estimating fractal parameters of Titan's surface.

1 INTRODUCTION

The Cassini Radar [1], [2] is a multimode instrument designed to investigate the inaccessible surface of Titan, Saturn's largest moon. The instrument operates on board the Cassini-Huygens Mission, an international project involving NASA, ESA and ASI (Agenzia Spaziale Italiana). The Altimeter Mode aims to study the relative topographic change of Titan's surface along sub-satellite tracks.

Before the Cassini Mission, spaceborne radar altimeters have been commonly used on Earth to map Earth's geoid, to study oceanic processes, to obtain topographic details of ice, land and sea surfaces, to monitor and collect data concerning various global processes [10].

It is well known that the characteristics of altimeter waveform are strongly related to surface statistical properties (i.e. roughness, rms slope, etc.). In principle, this means that the information content carried by a received echo can be extracted if we make use of a model of the altimeter's echo waveform.

In 1977, G. S. Brown proposed a theoretical model of the average impulse response of a rough surface, the so-called Brown's model, which has been widely applied to pulse-limited radar altimeters devoted to nadir ocean observations [8].

Due to mission constraints, the Cassini Radar Altimeter works so that pulsewidth-limited and beam-limited circles are comparable [13], [6]. In this situation, some general assumptions of conventional models are not applicable for Cassini Radar. Furthermore, the geometry involved, mainly the effective attitude of the Cassini orbiter during the hyperbolic Titan fly-bys and the not negligible off-pointing angles, strongly affects the waveform shape, and hence the final altimetric measurements. This implies the demand for a surface impulse response approximation of [7] which incorporates all those effects and admits a straight-forward closed form solution.

For off-nadir measurements, Brown [7] showed the FSIR (Flat Surface Impulse

Response) approximation by means of an asymptotic expression obtained by means of the Laplace's method, with an error lower than 2% of true value when dealing with far off-nadir pointing angles [16].

Using the same hypotheses made by Brown in [8], but with a different approach, [13] made a model based on a series expansion of the Bessel function, not dependent on the radar operating condition and also suitable in case of large mispointing. However, the final numerical expression makes difficult the implementation of any parametric estimation procedures.

Surface Titan profile obtained by processing Cassini altimetric data has been also analyzed showing its fractal behavior [3].

Following a short description of Cassini altimetric Mission, a new closed-form solution for altimeter waveform to be used in case of near-nadir measurements is presented. A comparison with respect to ocean-type Brown's model is also showed. Model related error budget has been assessed with respect to numerical solution. The developed analytical model is exploited to estimate surface height and sigma nought by means of a Maximum Likelihood (ML) method. The implemented algorithm is described and its performance are evaluated by means of simulated echoes of Cassini Radar in altimeter mode.

2 SATELLITE ALTIMETRY

Altimeters are active microwave instruments for the accurate measurement of vertical distances (between the spacecraft and the altimeter footprint). The technology determines the two-way delay of the radar pulse echo from the Earth's surface to a very high precision (to less than a nanosecond). The concept has also the capability to measure the power and the shape of the reflected radar pulses.

Since the first dedicated altimeter was launched on Seasat platform in 1978, satellite altimetry has lived an incredible and continuous development as long as new sensors were designed and became operational. The accuracy in range measurements gradually reached values that have allowed an extraordinary increase in our knowledge of many aspects of ocean and ice dynamics and variability. A summary of important characteristics for some past and future spaceborn altimeter missions is given in the following.

Mainly, the evolution of the altimeter transmitter is marked by improvements in pulse compression techniques that have substantially reduced peak power requirements. All the altimeter missions below introduced operate at Ku-Band. The choice of frequency is constrained by both the system and operational requirements. Since a narrow transmitted pulse is required to achieve a reasonable range precision, high frequency operation will support both the large receiver bandwidth and narrow antenna beamwidth requirements. The upper limit on the operational frequency is constrained by atmospheric attenuation effects that significantly degrade the performance of the altimeter for frequencies $> 18\text{GHz}$. In some altimetric missions, for instance Topex, the radar altimeter instrument includes C-Band transmitter so that ionospheric propagation delays can be accurately measured. Generally, the two-frequency system will produce a sub-decimeter range precision so that very small variations (particularly in ocean surface) can be detected.

ERS: the first European satellite to carry a radar altimeter, ERS-1, was launched on 17 July 1991. This satellite was designed to have different orbital configurations. During the first few months, the Commissioning Phase, all instruments were calibrated and validated. Since then, ERS-1 has been flying two Ice Phases (in which the repeat period was 3 days), a Multi-Disciplinary Phase (a 35-day repeat orbit lasting from April 1992 till December 1994), and the Geodetic Phase, which started in April 1994 and had a repeat period of 168-days. The second repeat cycle in this Phase, till the launch of ERS-2, was shifted by 8 km with respect to the first, so a ``336-day repeat`` was obtained. ERS-2 was launched on 21 April 1995 and operated simultaneously to ERS-1, until ERS-1 was retired, in March 2000. Since their launch, ERS satellites have monitored the sea surface almost continuously. The accuracy of their altimeter range measurements has been estimated to be a little under 5 cm.

TOPEX/Poseidon: was launched in 1992 as joint venture between CNES and NASA. While a 3-year mission was initially planned, with a 5-year store of expendables, TOPEX/Poseidon is still flying, 9 years after its launch. Due to the low orbit inclination, data coverage is more limited respect to ERS data. However, TOPEX/Poseidon is equipped with two experimental altimeters, one French and one US-made, that reach an accuracy in sea surface height determination around 3 cm. Thanks to this high performance, for the first time, the seasonal cycle and other temporal variability of the ocean have been determined globally with high accuracy, yielding fundamentally important information on ocean circulation.

ENVISAT: in November 2001, the European Space Agency launched Envisat, an advanced polar-orbiting Earth observation satellite which is still providing measurements of the atmosphere, ocean, land, and ice over a several year period. The Envisat satellite has been designed to ensure the continuity of the data measurements of the ESA ERS satellites. A radar altimeter (RA-2) will

be mounted on Envisat. This instrument is derived from the ERS-1 and 2 Radar Altimeters, providing improved measurement performance and new capabilities determining the two-way delay of the radar echo from the Earth's surface to a very high precision, within 2.5 centimetres.

JASON-1: is the first follow-on to TOPEX/Poseidon mission. It was launched in 2001 and provided highly accurate ocean altimetry data and near-real time altimetry data for predicting sea state and ocean circulation. Built by CNES, Jason is a lightweight altimeter based on the experimental secondary altimeter used by TOPEX/Poseidon. A second system at microwave has been used to measure the density of water vapour in the atmosphere, which allowed much more accurate atmospheric corrections. This system was able to measure sea surface height to within 2.5 centimetres.

CRYOSAT 2: was the first satellite to be realized in the framework of the Earth Explorer Opportunity Missions of ESA's Living Planet Programme. The mission concept has been selected in 1999 with an anticipated launch in 2004. Cryosat 1 and following Cryosat 2 it is radar altimetry mission dedicated to observations of the Polar Regions. The goal is to study possible climate variability and trends by determine variations in thickness of the Earth's continental ice sheets and marine sea ice cover. The CryoSat2 Mission makes use of a near polar Low Earth Orbit (LEO) non sun-synchronous at an altitude of ~ 720 km with an inclination of 92 degrees. The spacecraft accommodates the Altimeter SIRAL, DORIS receiver and Laser reflector.

In spite of the big progress done, big improvements can be achieved both for what concerns an increase in the range measurements accuracy, that could allow a more precise description of sea surface topography especially for regions where dynamic signals are not particularly strong (as the Mediterranean sea), or thinking of more reliable measurements near the coasts, and finally identifying sampling strategies that could allow a more synoptic and global coverage of the Earth surface which is

fundamental for a precise monitoring of mesoscale currents.

The basic concept of satellite altimetry is deceptively straightforward. The principal objective is to measure the range R from the satellite to target surface. The altimeter transmits a short pulse of microwave radiation with pre-defined power toward the target surface. The pulse interacts with the rough surface and part of the incident radiation reflects back to the altimeter. The techniques for radar determination of the time t for the pulse to travel round trip between the satellite and surface are described in section 3. The range R from the satellite to surface is estimated from the round trip travel time by:

$$\hat{R} = R - \sum_j \Delta R_j \quad (1)$$

where $\hat{R} = ct/2$ is the range computed neglecting refraction based on free space speed of light c and $\Delta R_j, j=1, \dots, N$ are corrections for the various components of the atmospheric refraction and for biases between the mean electromagnetic scattering surface and mean reference target surface.

The range estimate (1) varies along the satellites orbit from along-track variations of both the surface topography (mainly sea-surface) and the orbit height relative to the centre of the Earth. For more accurate mission requirements, as oceanography, the range estimate must be transformed to a fixed coordinate system. As introduced in section 3, this is achieved by precision orbit determination of the height H of the satellite relative to a specified ellipsoid approximation of the geoid.

The range measurements are then converted to the height h of the target surface relative to reference ellipsoid by:

$$\hat{R} = H - \hat{R} = H - \hat{R} + \sum_j \Delta R_j \quad (2)$$

It is worth noting that, accurate estimates of R and H are not sufficient for oceanographic applications of altimeter range measurements. The target-surface height given by (2), relative to the reference ellipsoid, it is the overlapping of a number geophysical effect. In addition to the dynamic effect of geostrophic ocean currents that are of primary interest for oceanographic applications (see Fu-Cazenave, 2001), h is affected by undulation of the geoid about the ellipsoidal approximation, tidal heights variations and ocean surface response to atmospheric pressure loading. These effects on the sea-surface height must be removed from h in order to investigate the effect of geostrophic ocean currents.

While complicating altimetric estimation of range R , the alteration of the incident radar pulse by a rough surface (sea, land, terrain, ice) can be utilized to extract other geophysical information from the radar return.

A primary characteristic in design of an altimeter system is the area on the target surface over which the range from the altimeter to the reference surface height is measured. The footprint of an antenna is traditionally described in terms of the beam-limited footprint, defined to be the area on target surface within the field of view subtended by the beam width of the antenna gain pattern.

For a narrow-beam antenna, the antenna beam-width can be expressed as:

$$\gamma = 2 \tan^{-1} \left(\frac{r}{R} \right) \approx 2 \frac{r}{R} \quad (3)$$

where r is the footprint radius and R is the orbit range.

The limitation of the beam-limited altimeter design can be overcome by transmitting a very short pulse with duration of a few nanoseconds (pulse-limited configuration) from an antenna with a smaller diameter and correspondingly wider beamwidth. The qualitative difference between these two modes is that the illuminated area on the surface is determined by the antenna beamwidth or transmitted pulsewidth, respectively. In order to indicate which mode is being used, the geometry of the altimetry must be examined. Figure 1 shows a nadir oriented antenna operating above a mean surface from the altitude h . The antenna beamwidth is given as BW and the transmitted pulsewidth is PW . The diameter of the area of the circle on the surface that is within the beamwidth is:

$$d_B = 2h \tan \frac{BW}{2} \quad (4)$$

Furthermore, the area of the circle formed by the intersection of the leading edge of the pulse with the mean surface when the trailing edge just intersects the surface at nadir point has a diameter given by:

$$d_P = 2\sqrt{(h + cPW)^2 - h^2} \quad (5)$$

A diagram of the altimeter pulse interaction with a quasi-flat surface is shown in Figure 2. As the incident pulse strikes the surface, it illuminates a circular region that

increases linearly with time. Correspondingly, a linear increase in the leading edge of the return waveform occurs. After the trailing edge of the pulse has intersected the surface, the region back-scattering energy to the satellite becomes an expanding annulus of constant area. At this point, the return waveform has reached its peak and then begins to trail off due to the reduction of the off-nadir scattering by the altimeter's antenna pattern. For a rough surface as rough ocean surface, the leading edge of the return pulse will be "stretched" because scattering from wave crests (or rough-peaks more generally) precedes the scattering from the wave troughs as the pulse wavefront progresses downward. Thus, the width of the leading edge of the return pulse can be related the level of the target surface roughness.

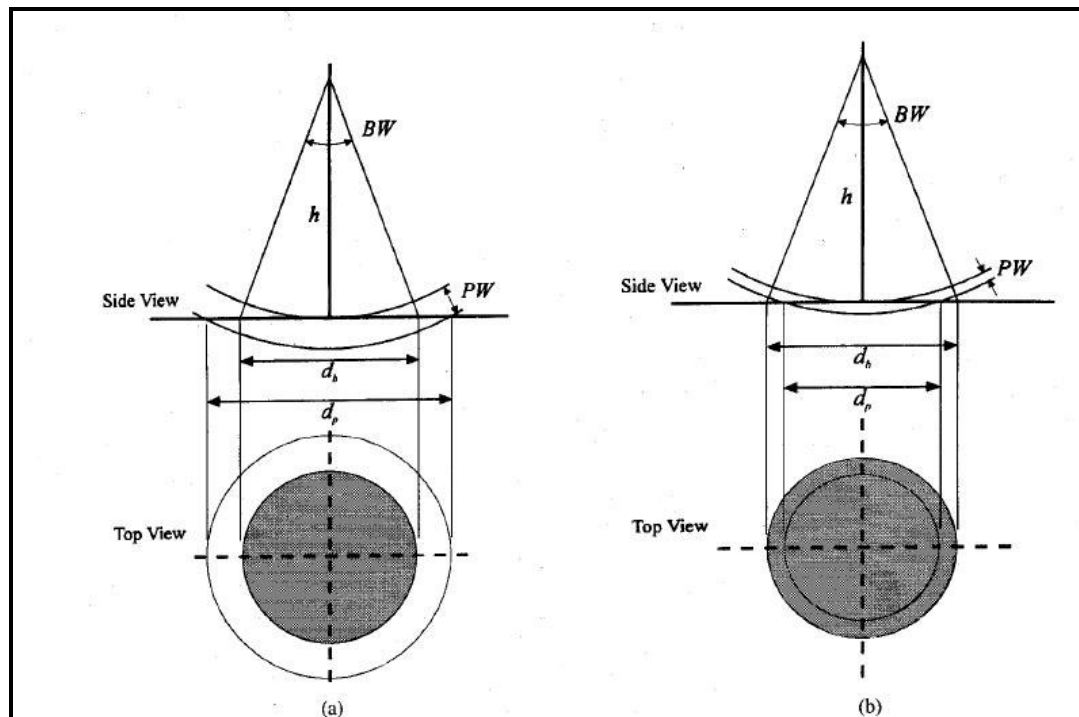


Figure 1 – Geometry of a nadir oriented (a) beamwidth-limited altimeter ($dP > dB$) and (b) pulsewidth-limited altimeter ($dP < dB$)

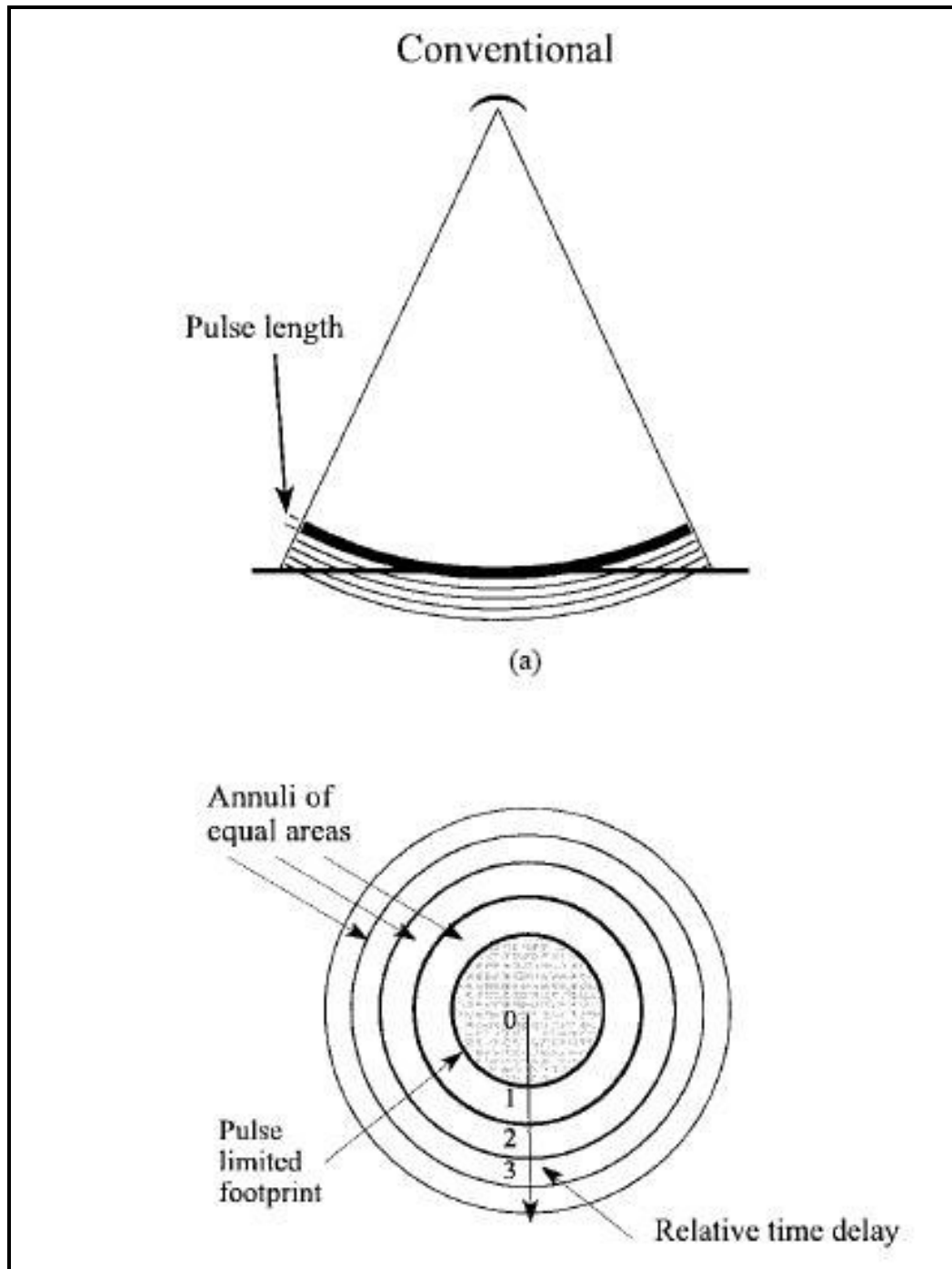


Figure 2 – Conventional Pulse Limited illumination geometry

3 THE CASSINI MISSION TO TITAN

Titan is the only satellite in the solar system with an appreciable atmosphere, composed mostly of Nitrogen, aerosols and a variety of hydrocarbons. Its surface is believed to feature chilled lakes of mainly methane, with a small amount of ethane, and a surface coated with sticky brown organic condensate that has rained down from the atmosphere [12]. Due to a dense hydrocarbon haze that forms in the stratosphere as methane is destroyed by sunlight, Titan's surface has been very difficult to study until now.

The Cassini Radar is a multimode microwave instrument that uses the 4 m high gain antenna (HGA) onboard the Cassini orbiter. The instrument operates at Ku-band (13.78 GHz or 2.2 cm wavelength) and it is designed to operate in four observational modes (Imaging, Altimetry, Backscatter and Radiometry) at spacecraft altitude below 100.000 Km, on both inbound and outbound tracks of each hyperbolic Titan flyby, and to operate over a wide range of geometries and conditions [2]. The instrument has been designed to have a wide range of capabilities in order to encompass a variety of possible surface proprieties.

From signal to noise and data rate considerations, the ALT mode is planned to operate at S/C altitudes between 4000 and 9000 Km, approximately from 16 minutes before the closest Titan approach of each Titan flyby until 16 minutes after the closest encounter. The Altimeter operates on "burst mode", similar to the imaging mode. When the ALT mode is executed, bursts of frequency modulated pulse signals (chirp pulses) of 150 μ s time duration and at 5 MHz bandwidth will be transmitted in a Burst Period (the Burst Repetition Interval is 3333 ms). The transmit time varies from 1.4 to 1.8 μ s. The number of pulses transmitted in each burst will vary throughout a single flyby pass.

During such operation, the radar utilizes the central, nadir-pointing antenna beam (Beam 3, a circular beam 0.350° across) for transmission and reception of chirp pulse signals ([1] and [2]).

The collected altimeter measurements are expected to have horizontal resolutions ranging between 24 and 27 Km, while the accuracy in estimating the relative surface elevation (that is, the change in local surface elevation relative to a reference datum) depends also on the topographic relief of the surface as well as on the knowledge of the spacecraft's ephemeris and attitude.

Instrument nominal main parameters used for the purpose of the present work are summarized in Table 1.

If we consider the nominal operating altitudes of the Cassini orbiter, we find that the radius of the pulsewidth-limited and of the beamwidth-limited circle are comparable, according with [13]. For instance, considering a nominal altitude of 6000 km we obtain, in the two cases, a footprint diameter of about 41.2 km and 36.5 km respectively.

Frequency	13.78 GHz
Antenna beamwidth (θ_{3dB})	0.350 deg (6.1 mrad)
Sampling frequency (f_c)	10 MHz
Chirp length (T)	150 μ s
Chirp bandwidth (B)	4.25 MHz
Range (vertical) resolution (ρ)	35.3 m

Table 1 – Main parameter for the HI-RES CASSINI altimeter

4 WAVEFORM MODEL DEVELOPMENT

The general assumptions at the basis of the development of the altimeter echo model hereafter described are [8]:

1. completely noncoherent nature of the scattering mechanism [15];
2. independent scattering elements on the observed surface;
3. rough surface with Gaussian height probability density function;
4. backscattering cross section per unit scattering area (σ_0) depending only on incidence angle;
5. negligibility of Doppler frequency spreads;
6. antenna beam circularly symmetric with Gaussian antenna gain pattern with respect to off-nadir angle θ , i.e.

$$G(\theta) \approx G_0 \exp\left(-\frac{2}{\gamma} \sin^2 \theta\right) \quad (6)$$

$$\gamma = -\frac{2 \sin^2(\theta_{3dB}/2)}{\ln(0.5)} \quad (7)$$

where:

G_0 is the peak antenna gain (at boresight)

θ_{3dB} is the -3 dB antenna aperture.

In order to obtain the average altimeter echo, for both nadir and off-nadir pointing observations, the convolution of the following three terms must be evaluated (convolutional model [14], [8]):

1. the FSIR (Flat Surface Impulse Response)
2. the radar point target response
3. the probability density function of the height of the specular points on the observed rough surface.

The expression of the FSIR including the radar mispointing (ξ) is given by [8] as a function of the two-way incremental ranging time $\tau=t-2h/c$:

$$\begin{cases} P_{FS}(\tau) = K_{FS} \exp\left(-\frac{4c\tau}{\gamma h \Lambda} \cos 2\xi\right) I_0\left(\frac{4}{\gamma} \sin 2\xi \sqrt{\frac{c\tau}{h\Lambda}}\right) & \tau \geq 0 \\ P_{FS}(\tau) = 0 & \tau < 0 \end{cases} \quad (8)$$

where:

$$K_{FS} = \frac{G_0^2 \lambda^2 c \sigma_0(\psi_0)}{4(4\pi)^2 L_p h^3} \exp\left(-\frac{4}{\gamma} \sin^2 \xi\right) \quad (9)$$

$$\psi_0 \approx \tan^{-1}(\sqrt{c\tau/h}) \quad (10)$$

Here c is the speed of light, λ is the radar carrier wavelength, L_p is the two-way path loss, h is the satellite altitude above the mean flat surface, and σ_0 is only dependant on the observation angle ψ_0 that can be neglected in case of small observation angles (i.e. σ_0 is constant over the effective illuminated area). As far as the last assumption is concerned, it is worth noting that, even the incidence angle is affected by local terrain slope and satellite attitude, models for electromagnetic scattering from natural

rough surfaces show negligible variation of σ_0 (tenths of decibel) up to few degrees [5]. The last expression is valid for:

$$\sqrt{\frac{c\tau}{h}} \tan \xi \ll 1 \quad (11)$$

that is well verified in the case of Cassini fly-bys. The only difference with respect to the classical formulation of Brown is the inclusion of the spherical surface effects that implies [16] a formal substitution of τ with τ/Λ , being:

$$\Lambda = (1 + h/R_T) \quad (12)$$

where R_T is the mean radius of Titan (2575 km).

Provided that P_T is the peak transmitted power, B and T are the transmitted bandwidth and pulse width, the system impulse response (IR) can be evaluated by taking the convolution of the FSIR with the convolution P_{HI} between the height probability density function and the system point target response, both supposed to be Gaussian:

$$P_{HI}(\tau) = K_{HI} \exp\left[-\frac{(\tau - \tau_0)^2}{2\sigma_c^2}\right] \quad (13)$$

where:

$$K_{HI} = P_T B T \sqrt{2\pi} \frac{\sigma_p}{\sigma_c} \quad (14)$$

$$\sigma_c = \sqrt{\frac{4}{c^2} \sigma_h^2 + \frac{1}{8 \ln 2 B^2}} \quad (15)$$

with the parameter σ_c related to either the rms height of the specular points relative to the mean reference surface (σ_h) and to system vertical resolution ($1/2B$).

In the last expression the extra delay τ_0 takes into account the time shift of height given, as sketched in Figure 3, by:

$$\tau_0 \approx \frac{2}{c}(h + R_T)(\cos \xi - 1) + \frac{(h + R_T)^2 \sin^2 \xi}{cR_T} \quad (16)$$

Of course, the extra delay τ_0 vanishes for nadir pointing altimetry, i.e. for $\xi=0$. In the following all the evaluated impulse response functions have to be considered delayed by the previous extra amount of time.

The convolution integral can not be solved analytically in the general case, except if a nadir pointing configuration is considered $\xi=0$. In this case, after some manipulation [4], the IR becomes:

$$IR^{Nadir}(\tau) = P_{FS}(\tau)|_{\xi=0} * P_{HI}(\tau) \quad (17)$$

$$IR^{Nadir}(\tau) = K\sigma^0 \frac{1}{2} \exp\left(-\frac{\delta}{\sigma_c}\tau + \frac{\delta^2}{2}\right) \left[1 + \operatorname{erf}\left(\frac{\tau}{\sqrt{2}\sigma_c} - \frac{\delta}{\sqrt{2}}\right)\right] \quad (18)$$

where:

$$K = \frac{G_0^2 \lambda^2 c P_T T}{32\pi \sqrt{8 \ln 2} L_p h^3} \quad (19)$$

$$\delta = \frac{4c}{\gamma h \Lambda} \sigma_c \quad (20)$$

Further details of calculation can be found in Appendix A.

The above equation can be considered as a generalization of the classical Brown's model [8]. In fact, it corresponds exactly to the Brown's solution if the argument of the erf function can be simplify, i.e.:

$$\frac{\tau}{\sigma_c} \gg \delta \quad (21)$$

The last expression, if verified for the minimum time delay ($\tau_{\min}=1/B$) and for flat surface ($\sigma_s=0$), can be rewritten as:

$$\frac{4c}{\theta_{3dB}^2 Bh} \ll 1 \quad (22)$$

which is the pulse-limited condition.

In case of an off-nadir pointing radar altimeter ($\xi \neq 0$), the FSIR evaluation cannot be simplified. The most practical method of evaluation of the average return power waveform should be numerical integration of the general expression given by [16].

When dealing with far off-nadir pointing angles, a closed asymptotic form for the FSIR can be derived [7] by using Laplace's method [17]:

$$P_{FS}^{Asymp}(\tau) = \frac{G_0^2 \lambda^2 c \sigma^0(\psi_0)}{2(4\pi)^3 L_p h^3} G(\varepsilon) \quad \tau \geq 0 \quad (23)$$

where:

$$G(\varepsilon) = \exp\left(-\frac{4(\sin \xi - \varepsilon \cos \xi)^2}{\gamma(1+\varepsilon^2)}\right) \sqrt{\frac{2\pi}{a+2b}} \quad (24)$$

$$a = \frac{4\varepsilon \sin 2\xi}{\gamma(1+\varepsilon^2)}, \quad b = \frac{4\varepsilon^2 \sin^2 \xi}{\gamma(1+\varepsilon^2)} \quad (25)$$

$$\varepsilon = \sqrt{\frac{c\tau}{h\Lambda}} \quad (26)$$

For high values of off-nadir angle the asymptotic expression of FS waveform becomes much wider than both the surface height distribution and the pulse response.

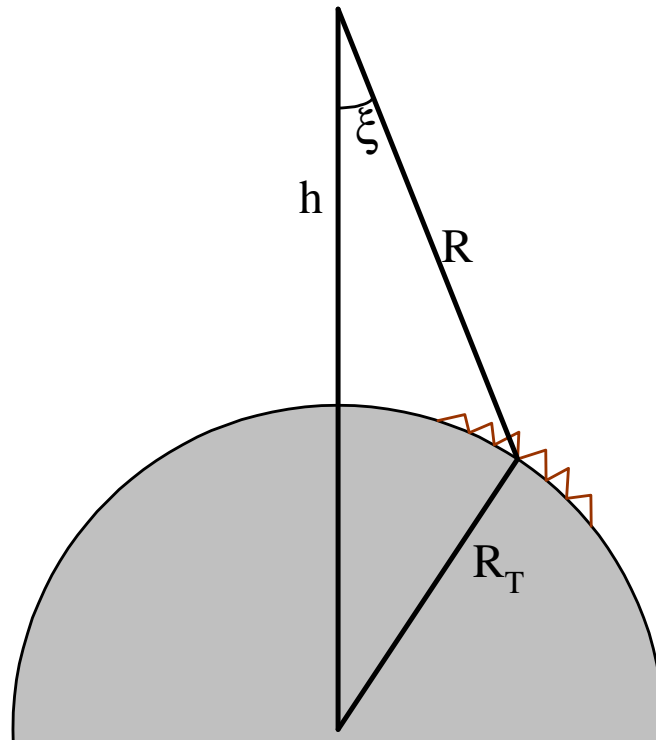


Figure 3 – Off-nadir altimetry geometry

Therefore, the total impulse response can be simply written as the following product:

$$IR^{Asym}(\tau) = \frac{K\sigma^0 G(\varepsilon)}{2} \left[1 + \operatorname{erf} \left(\frac{\tau}{\sqrt{2}\sigma_c} \right) \right] \quad \tau \geq 0 \quad (27)$$

The problem of finding a closed form for the impulse response still exists for small mispointing angles. A possibility, also suggested by Brown [8], consists in approximating the FSIR by a series of exponentials by using the classical Prony's method [11].

That approach is followed in this work, where only the Bessel function has been approximated by using Prony's method. In fact, by transforming the Bessel function of the FSIR to an appropriate exponential function allows to close the convolution integral.

The starting point is the FSIR expression of (8), that can be rewritten as a function of the non-dimensional parameter ε :

$$P_{FS}(\varepsilon) = K_{FS} \exp \left(-\frac{4}{\gamma} \varepsilon^2 \cos 2\xi \right) I_0 \left(\frac{4}{\gamma} \varepsilon \sin 2\xi \right) \quad \varepsilon \geq 0 \quad (28)$$

After some trade-off, it has been found that the most convenient way of approximating the Bessel function is the following:

$$I_0 \left(\frac{4}{\gamma} \varepsilon \sin 2\xi \right) \approx \sum_{i=1}^N C_i \exp[a_i x] \quad (29)$$

$$x = 4 \sin(2\xi) \varepsilon^2 / \gamma \quad (30)$$

where the constants C_i and a_i are evaluated with Prony's method of order N.

In this way the FSIR can be written as a simple summation of N exponential terms, such as:

$$P_{FS}^{Prony}(\varepsilon) = K_{FS} \exp(-K_a \tau) \sum_{i=1}^N C_i \exp(K_i \tau) \quad (31)$$

where:

$$\begin{cases} K_a = \frac{4}{\gamma} \cos(2\xi) \frac{c}{h\Lambda} \\ K_i = \frac{4}{\gamma} \sin(2\xi) \frac{c}{h\Lambda} a_i \end{cases} \quad (32)$$

For example, with reference to the main system parameter of Table 1 and by considering an altitude of the spacecraft of 5000 Km and an off-nadir angle of 0.15°, Table 2 shows the amplitude and exponential factors computed by the Prony's approximation of all orders. It is worth noting that, in general, these factors can be complex, but conjugated in pairs. Therefore the FSIR is a combination of exponential and sinusoidal terms given by the real and imaginary parts of K_i respectively. As expected the overall summation of the N exponential terms gives real results.

	N=2	N=3	N=4	N=5
C_i	0.47-3.56j 0.47+3.56j	9.10 -4.05-0.91j -4.05+0.91j	1.30-19.73j 1.30+19.73j -0.80+4.90j -0.80-4.90j	54.52 -31.67-2.47j -31.67+2.47j 4.91+0.32j 4.91-0.32j 29.65
a_i	50.01+22.69j 50.01-22.69j	43.98 31.58+27.76j 31.58-27.76j	33.35+9.73j 33.36-9.733j 19.86+24.94j 19.86-24.94j	25.32+13.55j 25.32-13.55j 13.18+21.94j 13.18-21.94j

Table 2- Exponential and amplitude factors for Prony's approximation

Now the convolution integral can be evaluated as done for equation (18). In an analogous way the following parameter can be defined:

$$\delta_i = (K_a - K_i) \sigma_c \quad (33)$$

and the final impulse response can be written as:

$$IR^{Prony}(\tau) = \frac{K\sigma^0}{2} \exp\left(-\frac{4}{\gamma} \sin^2 \xi\right) \cdot \sum_{i=1}^N C_i \exp\left(-\frac{\delta_i}{\sigma_c} \tau + \frac{\delta_i^2}{2}\right) \left[1 + \operatorname{erf}\left(\frac{\tau}{\sqrt{2}\sigma_c} - \frac{\delta_i}{\sqrt{2}}\right)\right] \quad (34)$$

Following what was said before, the erf function of (34) should be extended to complex argument [4].

The above analytical equation allows for approximating the impulse response in case of near off-nadir pointing angles. In the case of the Cassini Radar, negligible approximation errors are reached with few terms (4 at the maximum), as shown in the following section. This allows an easy and rapid calculation of either the impulse function and its derivative needed for the MLE estimation procedure.

It is worth noting that, for all cases corresponding to equations (18), (27) and (34), the averaged impulse response can be written in the following way, by underlining the dependence of main surface parameters:

$$IR^M(\tau) = A(\sigma^0) f_M(t_0, \xi, \sigma_s) \quad (35)$$

Some examples of such calculations and a full assessment of errors involved by the previous models are contained in the next paragraph.

5 MODELS ERROR BUDGET

In the previous paragraph three different models in analytical closed form have been formulated, corresponding to equations (18), (27) and (34). Only the last two models have been developed originally by the authors of the present work.

The aim of the present paragraph is to show some examples of model calculation and to assess errors with respect to the expected spacecraft altitude and off-nadir angle values of Cassini mission.

Relative errors are evaluated with respect to theoretical impulse response that is just the convolution of (8) with (13), i.e.:

$$IR^{Theo}(\tau) = \int_0^{+\infty} P_{FS}(\tau') P_{HI}(\tau - \tau') d\tau' \quad (36)$$

where the convolution integral is computed numerically.

For example, with reference to the main system parameter of Table 1 and by considering an altitude of the spacecraft of 5000 Km and an off-nadir angle of 0.15° , Figure 4 shows the corresponding normalized theoretical impulse response, evaluated for various surface height r.m.s values ($\sigma_h=10\text{m}$; 50m ; 100m). With respect to this reference curve and by considering $\sigma_h=10\text{m}$ as a reference value, Figure 5 shows the relative errors, in percentage, for all models. These results prove that also with low off-nadir angle the nadir model can not be used, whereas the Prony models gives negligible errors also with few terms ($N=2$ or $N=3$). More terms ($N=4$, $N=5$) do not add any improvement. As expected, also the asymptotic model gives very high errors.

The mean integral relative error (MIRE) has been evaluated and reported in Table 3 for all models and for $\sigma_h=10\text{m}$. This is the integral value of the relative errors of Figure 5, averaged over the time interval where the theoretical normalized impulse response is significant ($>1\text{e-}3$). This parameter has been chosen as the full indicator of the goodness of the model and it will be used in the following.

In order to examine the behavior of models as a function of spacecraft altitude in the nominal Cassini altimeter range, the MIRE has been evaluated for the same off-nadir angle and reported in Figure 6.

As expected, the values of Figure 6 follow those of Table 3, being high for the nadir and asymptotic models and very low for Prony's approximation, for which no improvements can be noted with more than three terms.

But Figure 6 is interesting for another reason, since it shows that the model's errors are almost independent of spacecraft altitude, at least in the Cassini altimeter operating range.

The main dependence is instead on off-nadir angle and it is summarized in Figure 7, where MIRE is plotted for all models. Figure 7 can also be used to fix threshold off-nadir values for switching among models, by using the crossing point between models and a criterion of a MIRE less than 1%. The evaluated threshold values and the corresponding model to be used are shown in Table 4.

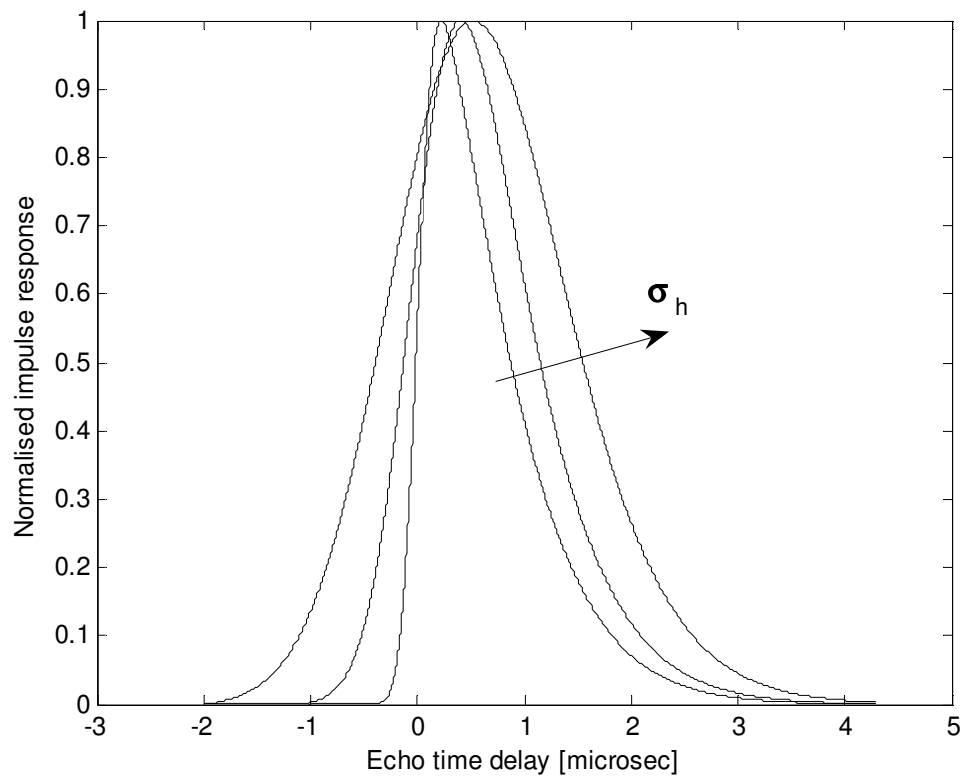


Figure 4 - Theoretical impulse response ($H=5000$ Km, $\xi=0.15^\circ$) for various surface height r.m.s. values ($\sigma_h=10\text{m}$; 50m ; 100m)

Nadir	Prony				Asymptotic
	N=2	N=3	N=4	N=5	
11.471	0.113	0.027	0.026	0.026	2.829

Table 3 - Mean integral relative error for all models

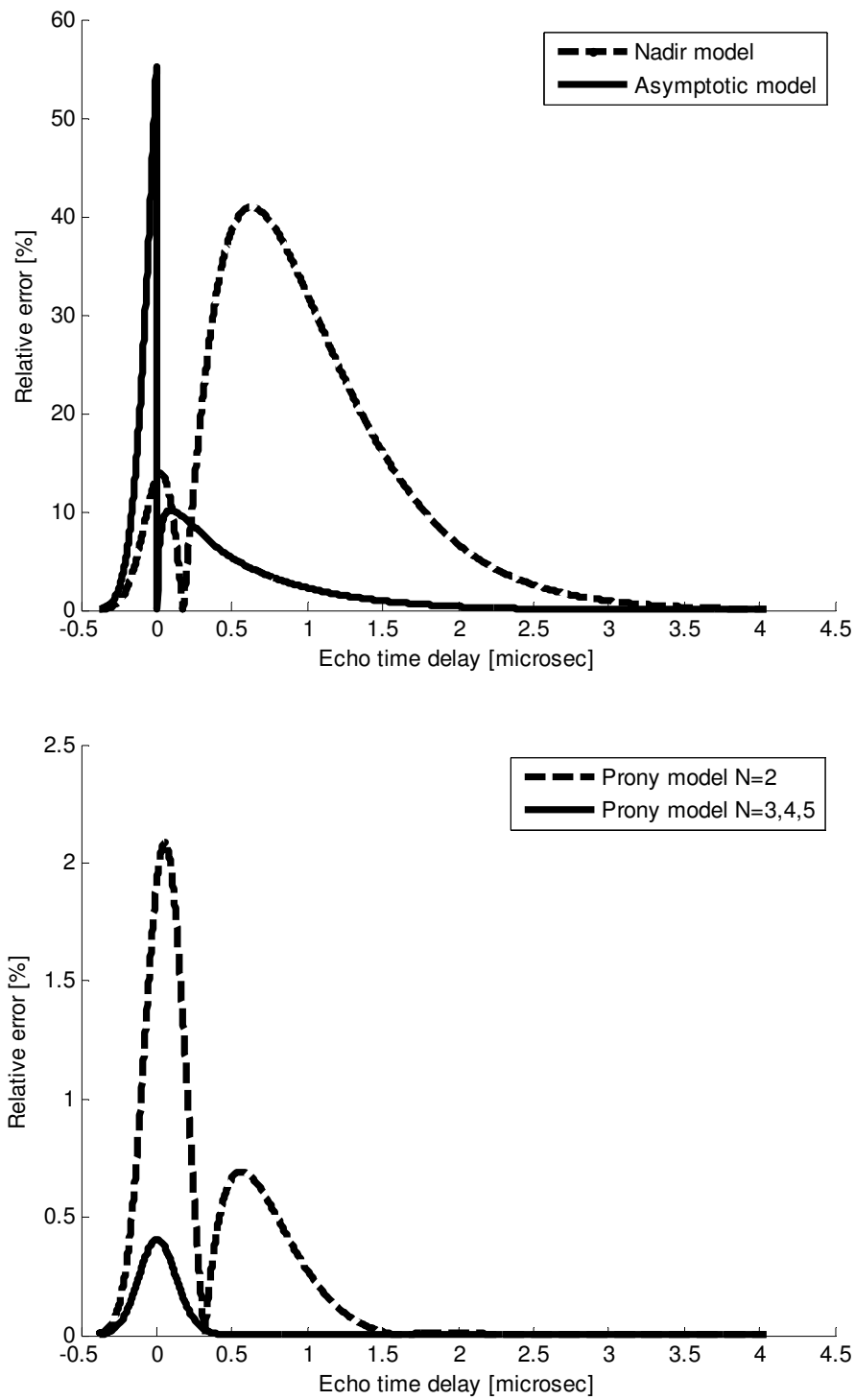


Figure 5 - Relative errors for all models ($H=5000$ Km, $\xi=0.15^\circ$)

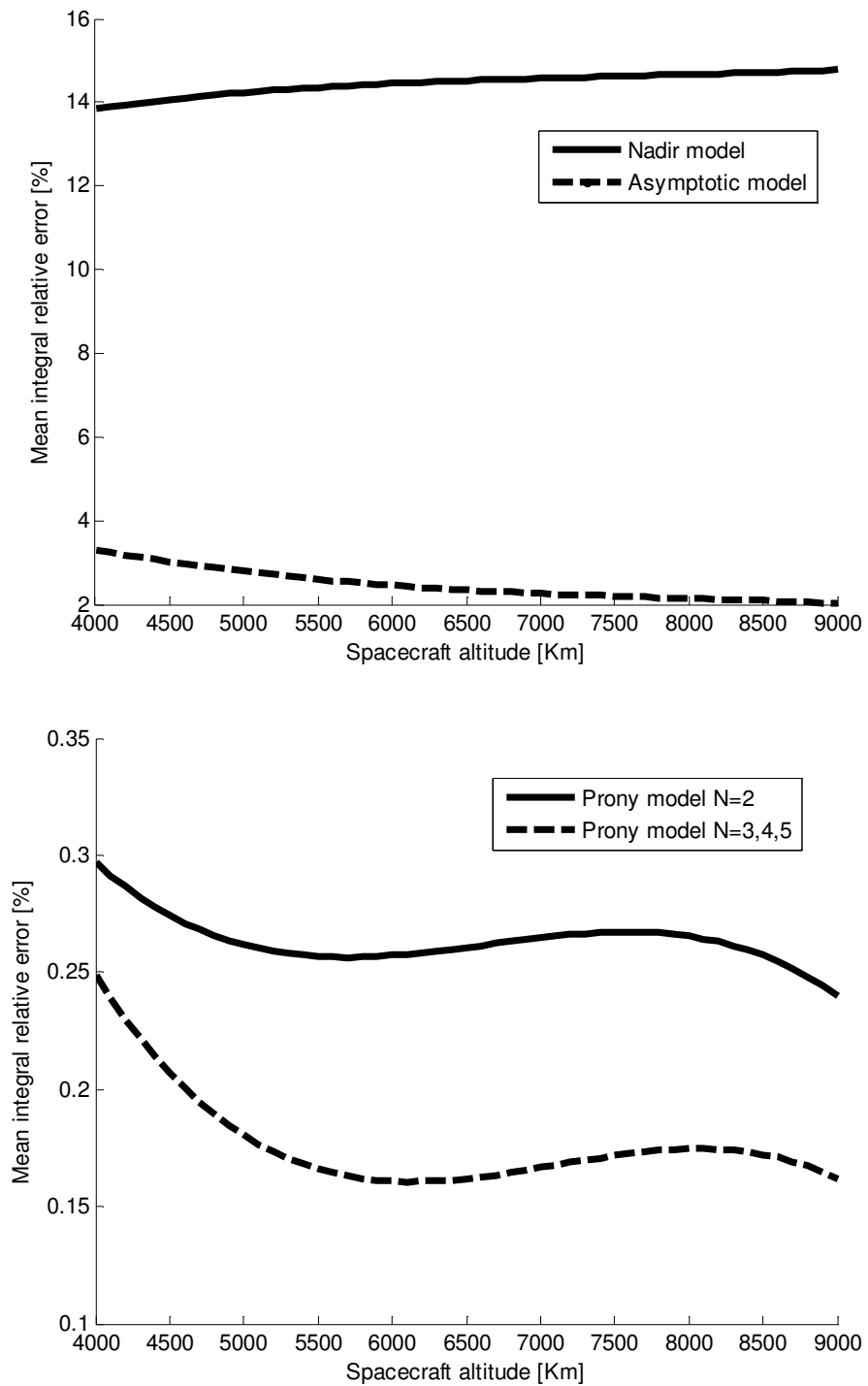


Figure 6 - Mean integral relative error for all models as a function of spacecraft altitude ($\xi=0.15^\circ$)

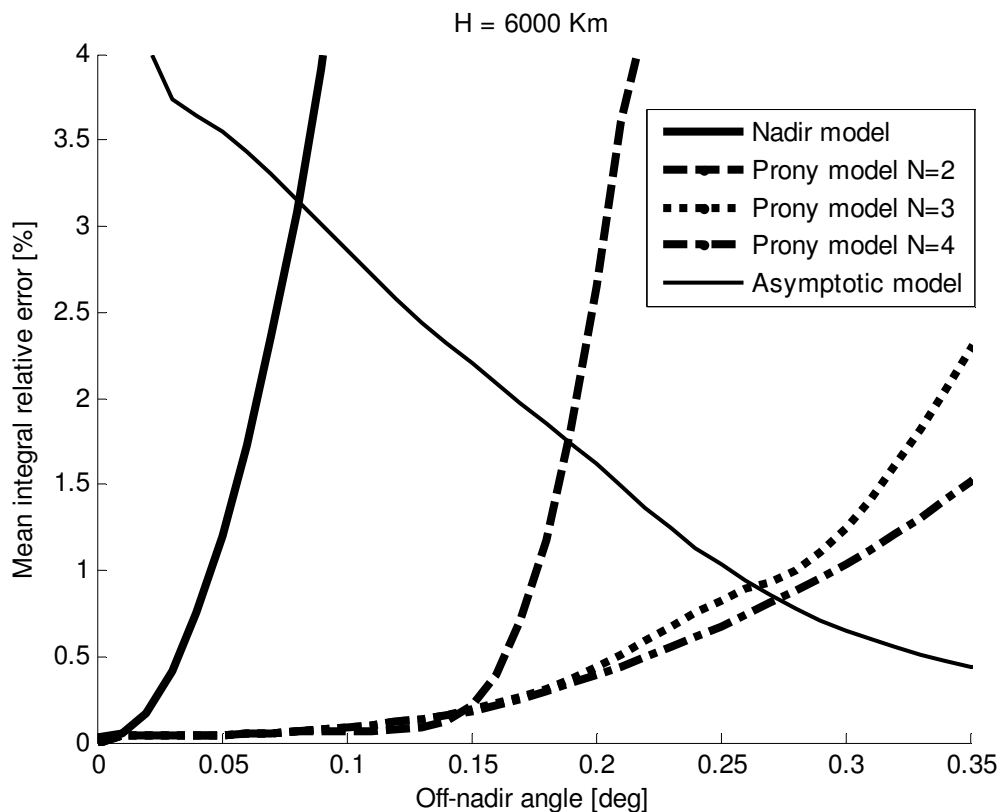


Figure 7 - Mean integral relative error for all models as a function of off-nadir angle (H=6000 Km)

Threshold off-nadir angle [deg]	Model to be used
$0 < \xi < 0.04$	Nadir
$0.04 \leq \xi < 0.16$	Prony's N=2
$0.16 \leq \xi < 0.26$	Prony's N=3
$0.26 \leq \xi < 0.29$	Prony's N=4
$\xi \geq 0.29$	Asymptotic

Table 4 – Threshold values for off-nadir angle and corresponding model for assuring a MIRE less than 1 %

6 HEIGHT RETRIEVAL ALGORITHM

In the previous paragraphs an analytical approximated form of the averaged impulse response has been found and its validity in case of Cassini radar altimeter has been studied. The analytical expression depends on either system (such as off-nadir angle, transmitted bandwidth, antenna aperture and gain, spacecraft altitude, etc.) and terrain (such as mean and root mean squared height, sigma nought, etc.).

In the present paragraph the “inverse” problem will be treated, that is the estimation of such parameters from real data acquired by the radar, that are affected by thermal noise and, mainly, by speckle.

This is a classical problem in the linear estimation theory and several methods exist for inferring parameters of the underlying probability distribution from a given data set.

Among these the maximum likelihood estimation (MLE) exhibits several characteristics which can be interpreted to mean that it is "asymptotically optimal" since it is asymptotically unbiased (its bias tends to zero as the number of samples increases to infinity) and it is asymptotically efficient, i.e., it achieves the Cramér-Rao lower bound when the number of samples tends to infinity [18]. This means that, asymptotically, no unbiased estimator has lower mean squared error than the MLE.

Given observations (x_1, \dots, x_N) depending on a set of parameters $(\theta_1, \dots, \theta_M)$ and affected by noise with known probability density function, the MLE searches for the parameter values that maximize the likelihood function:

$$L(\theta_1, \dots, \theta_M) = f_{\theta}(x_1, \dots, x_N / \theta_1, \dots, \theta_M) \quad (37)$$

In our case the compressed radar signal is digitized with a certain sampling frequency (f_s) and squared (power detected) so that each sample at a time $t_i = 1/f_s$ is indicated with D_i .

Therefore, each sample D_i is exponential distributed, with a mean equal to the i -th sample of the averaged impulse response evaluated by using (18), (27) or (34) according to the off-nadir angle with the threshold values of Table 4.

In addition, for each burst, N_B pulses are available (typically 15 for the high resolution altimeter mode) that can be exploited for making an incoherent summation before the height retrieval process start.

In this way, the i -th averaged sample D_i can be approximately view as Gaussian distributed with:

$$E[\bar{D}_i] = E[D_i] = IR_i \quad (38)$$

$$VAR[\bar{D}_i] = VAR[D_i]/N_B = IR_i^2/N_B \quad (39)$$

By supposing the samples independent, the likelihood function becomes a product of N Gaussian probability densities functions, such as:

$$L(\theta_1, \dots, \theta_M) = \prod_{i=1}^N \frac{1}{IR_i} \sqrt{\frac{N_B}{2\pi}} \exp\left[-\frac{N_B}{2IR_i^2} (\bar{D}_i - IR_i)^2\right] \quad (40)$$

The maximization of such a likelihood function can be more easily performed by taking the derivation of the logarithm of the likelihood function itself:

$$\frac{\partial}{\partial \theta_i} \ln(L) = 0 \quad (41)$$

where θ_i is the generic parameter to be estimated. The last expression can be reworded as:

$$\frac{\partial}{\partial \theta_i} \sum_{i=1}^N \left[\frac{1}{2} \ln \left(\frac{N_B}{2\pi} \right) - \ln (IR_i) - \frac{N_B}{2IR_i^2} (\bar{D}_i - IR_i)^2 \right] = 0 \quad (42)$$

With simple calculations and by considering M parameters to be estimated, the last expression entails the solution of the following non-linear system:

$$\begin{cases} \sum_{i=1}^N \frac{N_B \bar{D}_i^2 - N_B \bar{D}_i IR_i - IR_i^2}{IR_i^3} \frac{\partial IR_i}{\partial \theta_1} = 0 \\ \dots\dots\dots \\ \sum_{i=1}^N \frac{N_B \bar{D}_i^2 - N_B \bar{D}_i IR_i - IR_i^2}{IR_i^3} \frac{\partial IR_i}{\partial \theta_M} = 0 \end{cases} \quad (43)$$

The practical implementation of the MLE method differs from the last theoretical expression since its potential instabilities have to be managed. They are mainly due to the presence of amplitude terms in the expression of the derivatives of the model used that forces the use of simpler expressions for decoupling equations. To this end, the following sub-optimal strategy has been followed:

1. normalized derivatives have been used:

$$\overline{\frac{\partial IR_i}{\partial \theta_M}} = \frac{\partial IR_i}{\partial \theta_M} / \max \left(\frac{\partial IR_i}{\partial \theta_M} \right) \quad (44)$$

2. the IR_i^2 term has been neglected in the numerator, since it is not multiplied by N_B ;

3. the \overline{D}_i term of the numerator has been simplified with IR_i in the denominator, since they are equal in the average;
4. since low values of the remaining term IR_i^2 can cause instabilities in the estimate, denominator has been substituted with a constant term, given by:

$$C = \sum_{i=1}^N IR_i^2 \quad (45)$$

The final result for the actual implementation of the MLE method is therefore the following:

$$\begin{cases} \frac{1}{C} \sum_{i=1}^N (\overline{D}_i - IR_i) \frac{\partial IR_i}{\partial \theta_1} = 0 \\ \dots\dots\dots \\ \frac{1}{C} \sum_{i=1}^N (\overline{D}_i - IR_i) \frac{\partial IR_i}{\partial \theta_M} = 0 \end{cases} \quad (46)$$

Of course, the last MLE equations are solved iteratively, following the scheme shown in

Figure 8, where only the echo time delay τ_0 and the impulse response amplitude A are retrieved by using MLE method.

By solving the equations set, at the n -th iteration two errors are evaluated (namely $\varepsilon_\tau^n, \varepsilon_A^n$) and their values are used for updating the actual estimates to be used in the next iteration, as:

$$\begin{aligned} t_0^{(n+1)} &= t_0^{(n)} + \varepsilon_\tau^{(n)} \\ A^{(n+1)} &= A^{(n)} + \varepsilon_A^{(n)} \end{aligned} \quad (47)$$

The final values are reached when the two errors become lower than some fractions (0.01 for example) of signal sampling interval (200 nsec for CASSINI) and signal maximum amplitude.

Some words should be spent to discuss on the influence of off-nadir angle on MLE performance. This angle was not included, at the moment, in the MLE estimation but it is only used as a “perfect” parameter to generate impulse response and its derivatives. In other words, it was preferred to rely on a high degree of accuracy of spacecraft attitude control system instead of overloading the MLE procedure from a computational point of view, making the convergence more difficult. Nevertheless, there could be some other effects that would significantly affect the estimation performance such as the presence of local terrain slope that acts like an equivalent off-nadir angle. The final results on the received echo is a higher degree of echo time spread resulting in an increasing of received pulse width that, if not compensated, can degrade significantly the estimation performance. A method for managing this problem is correcting the off-nadir angle on the basis of the measured pulse width and following a relationship retrieved by using the analytical models. As a measure of received pulse width, the evaluation of signal second central moment can be used. Figure 9 shows the impulse response time width (second central moment) as a function of off-nadir angle for various spacecraft altitude values. The values have been evaluated on the basis of developed analytical models and they can be used for “adjusting” the off-nadir angle to be used for the MLE procedure.

The actual performance of the implemented method can be evaluated via simulation, since the Cramer-Rao bound can give optimistic values in this case.

Single Cassini radar pulses can be generated by evaluating the theoretical impulse response through numerical computation of convolution integral. These values are used to generate exponentially distributed variables, that represent a simulated radar echo. Following Cassini radar timing, fifteen echoes are therefore incoherently summed for simulating the averaged pulse obtained for each burst. An example of

the obtained results are shown in Figure 10.

The MLE algorithm has been applied to 1000 simulated bursts for each off-nadir angle and altitude values in the operating range of Cassini radar and the obtained statistical results are reported in Figure 11 and Figure 12 in terms of mean and standard deviation of error height and normalized sigma nought.

A critical aspect of the proposed method is the choice of initial guess of the estimation cycle, especially for low altitude and small off-nadir when the echo is expected to be very narrow.

To this aim, the followed strategy is based on integral measurements done on received data corrected by means of analytical models.

In more details, as far the time delay is concerned (t_0^i of Figure 8), for each averaged burst the centroid values is evaluated, i.e. the samples that balances the energies on right and left side. This values is then decreased by a factor evaluated by means of developed analytical models and that accounts for the difference between the true time delay and the centroid. The delay correction is shown in Figure 13 as a function of off-nadir angle and for various spacecraft altitude values.

The same procedure for evaluating the initial guess of echo amplitude, i.e. A_i of Figure 8 can be followed. Since the MLE algorithm works with normalized waveforms, the initial amplitude value should be chosen in order to fix the resulting model amplitude equal to one. This can be done by using the developed analytical model, as shown by Figure 14 where the initial values for getting a resulting model amplitude equal to one are plotted, as a function of off-nadir angle and for various spacecraft altitude values.

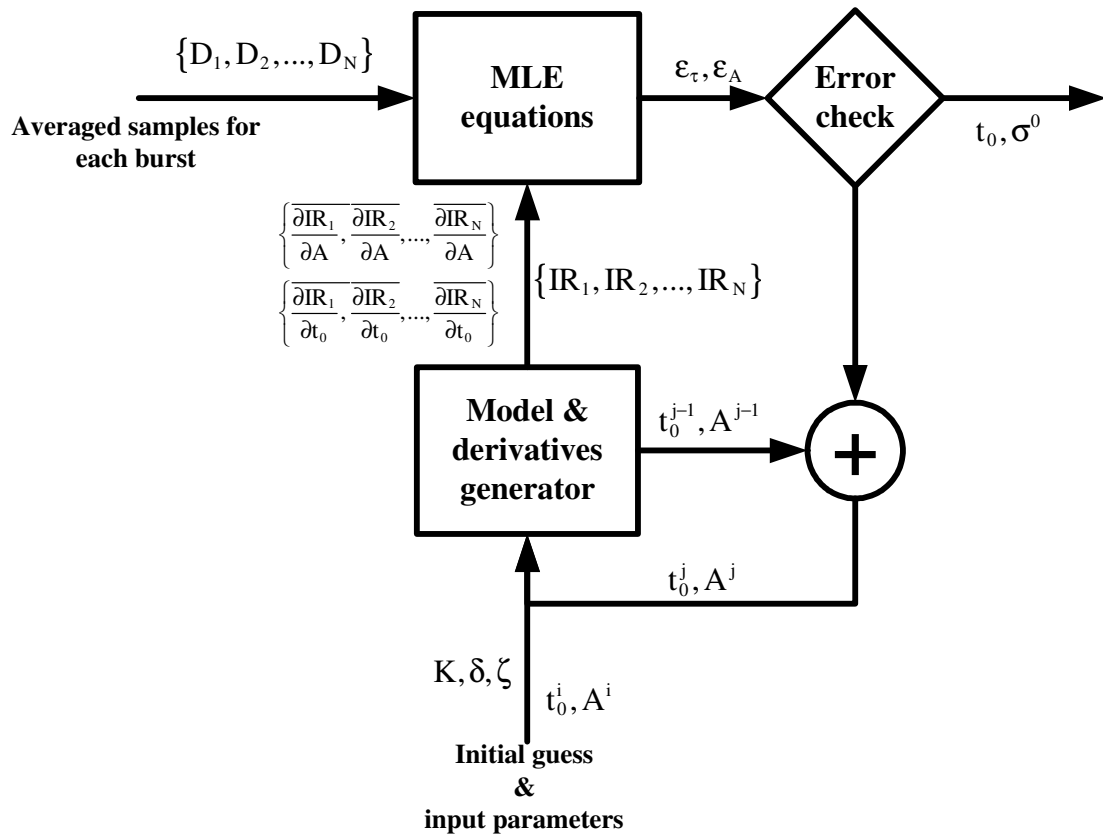


Figure 8 - Algorithm for actual implementation of MLE method

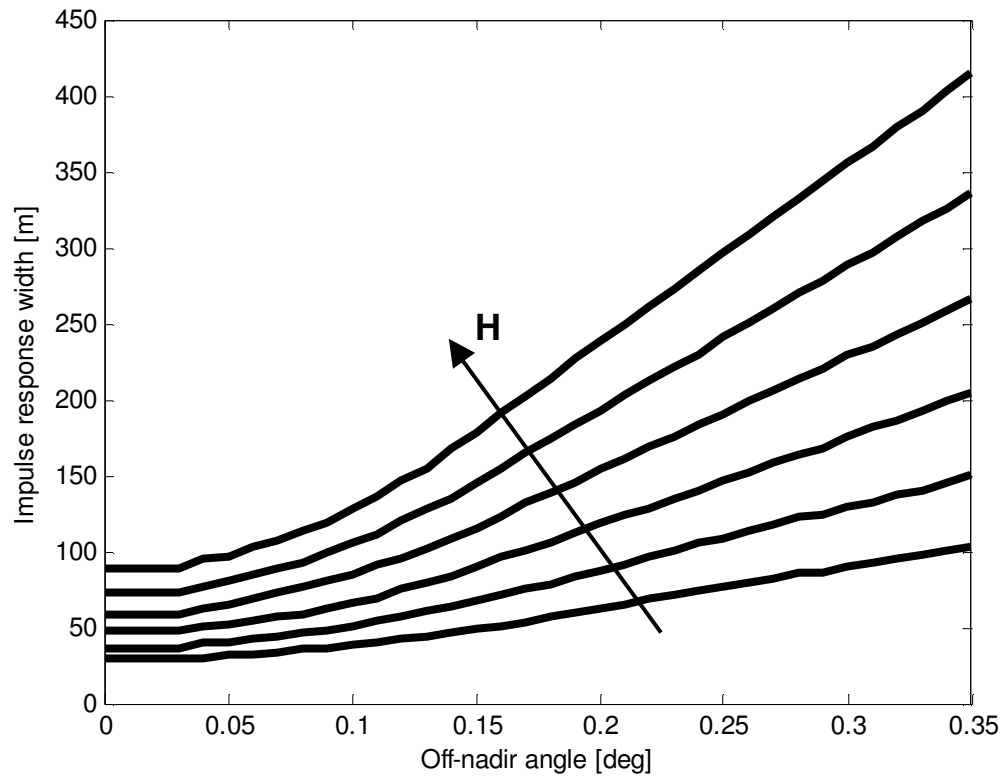


Figure 9 - Impulse response time width (second central moment) as a function of off-nadir angle for various spacecraft altitude (H) values (4000 Km up to 9000 Km, step 1000 Km). The values have been evaluated on the basis of developed analytical models and they are used for correcting the off-nadir angle to be used for the MLE procedure.

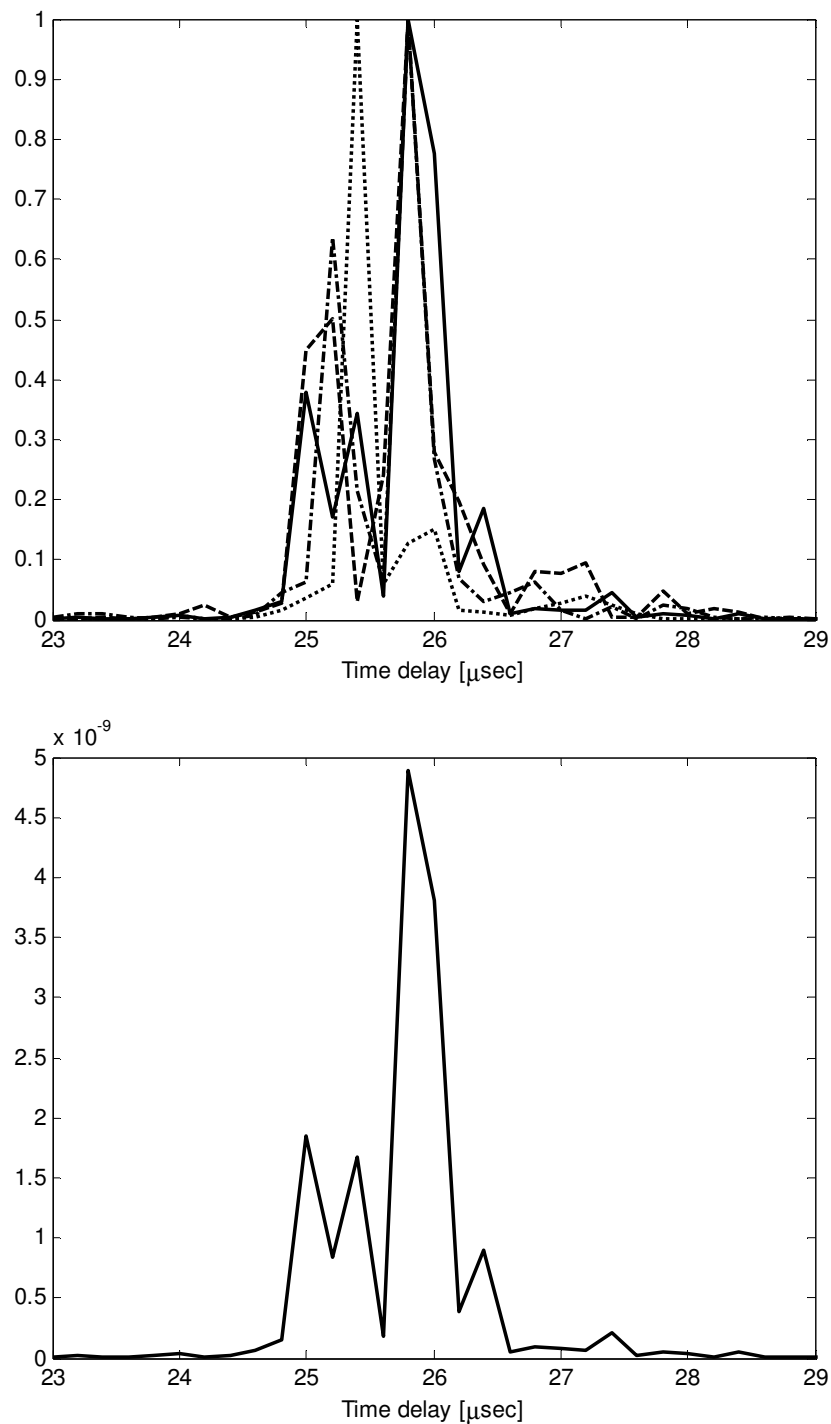


Figure 10 - Simulated Cassini radar echoes with $H=5000$ Km and $\xi=0.15^\circ$ - some realizations (top) and the averaged echo (bottom)

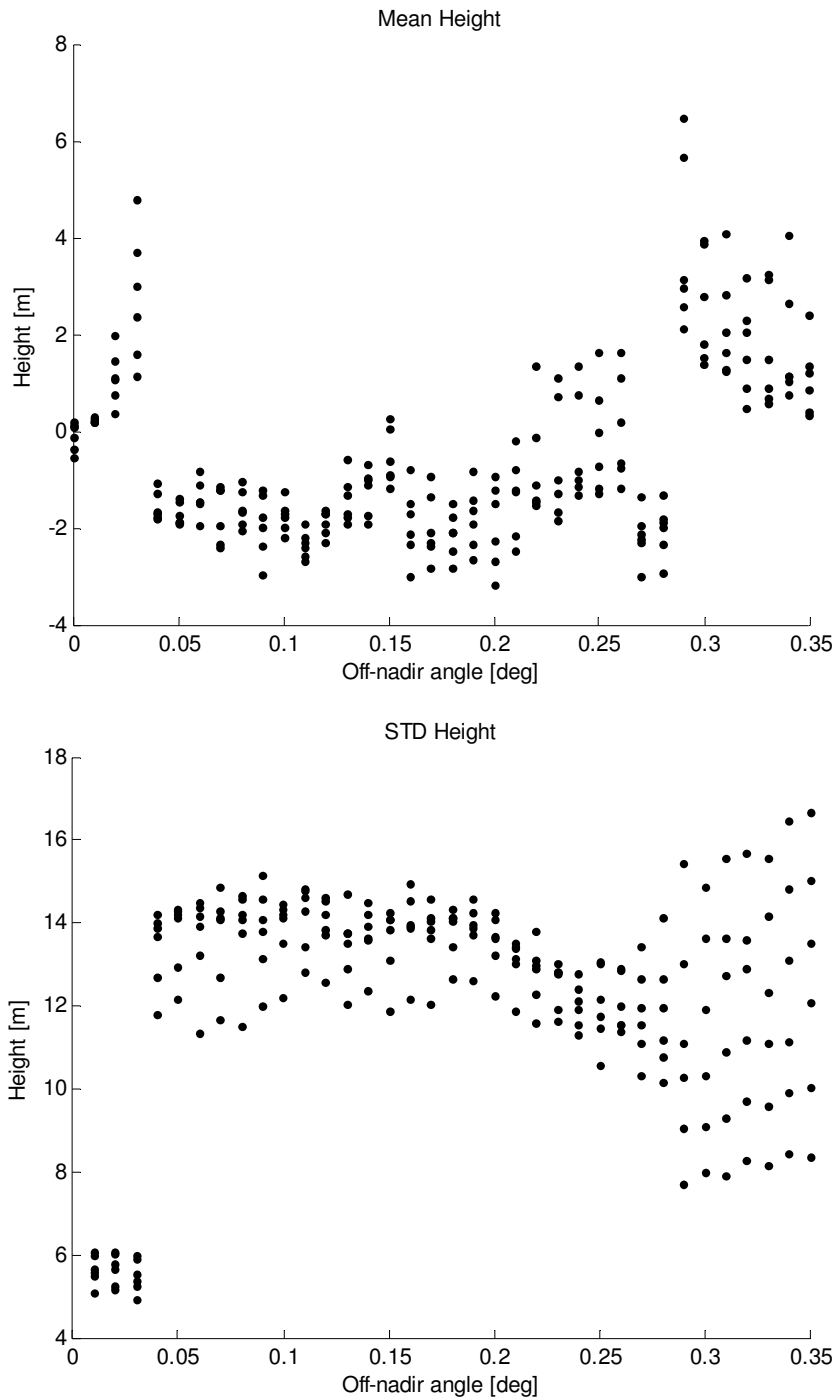


Figure 11 - Height error: statistical results obtained by applying the MLE algorithm (1000 simulations) as a function of off-nadir angle for various spacecraft altitude (4000 km up to 9000 km with 1000 km step) – mean (top) and standard deviation (bottom) values.

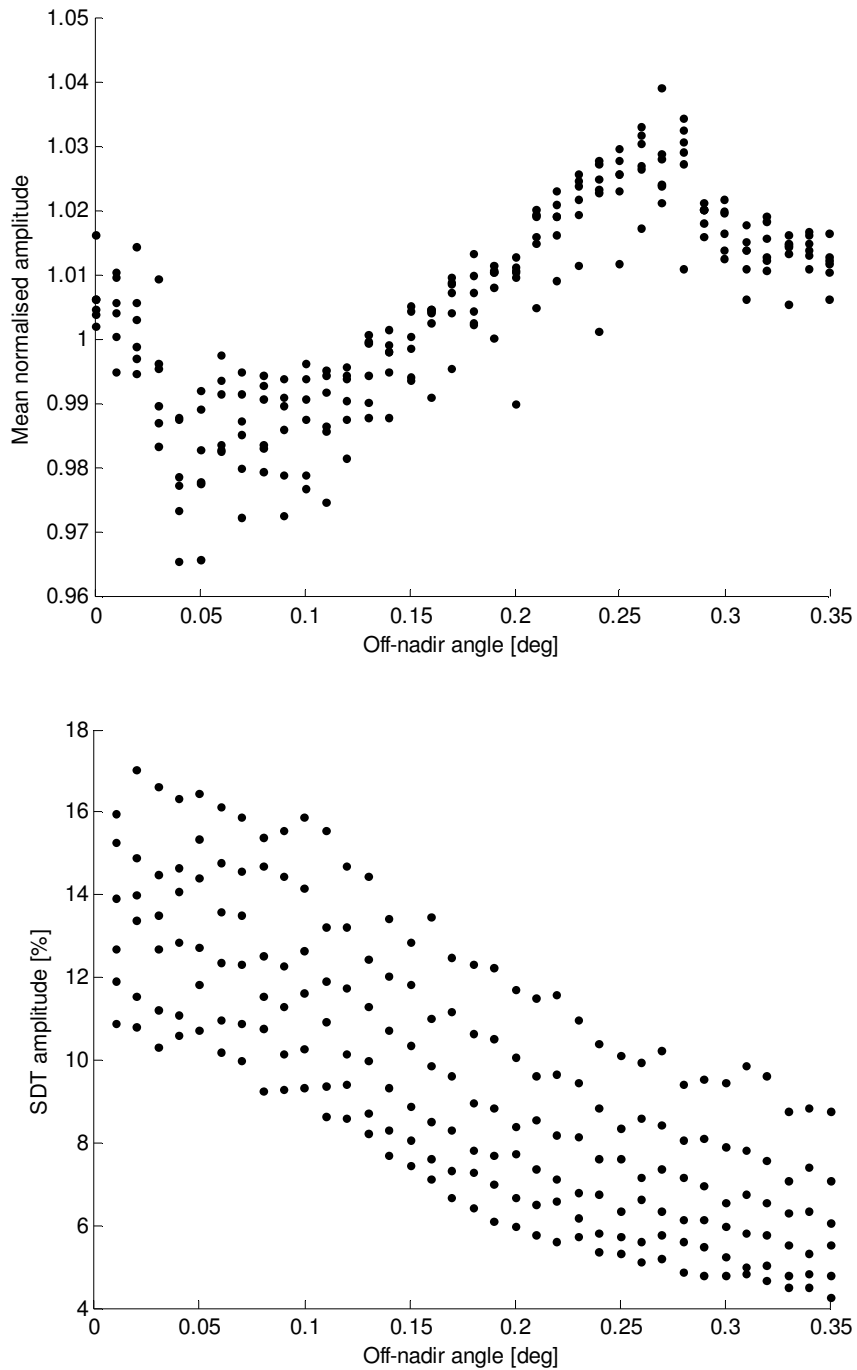


Figure 12 - Normalized sigma nought error: statistical results obtained by applying the MLE algorithm (1000 simulations) as a function of off-nadir angle for various spacecraft altitude(4000 km up to 9000 km, 1000 km step) - mean (top) and standard deviation (bottom) values.

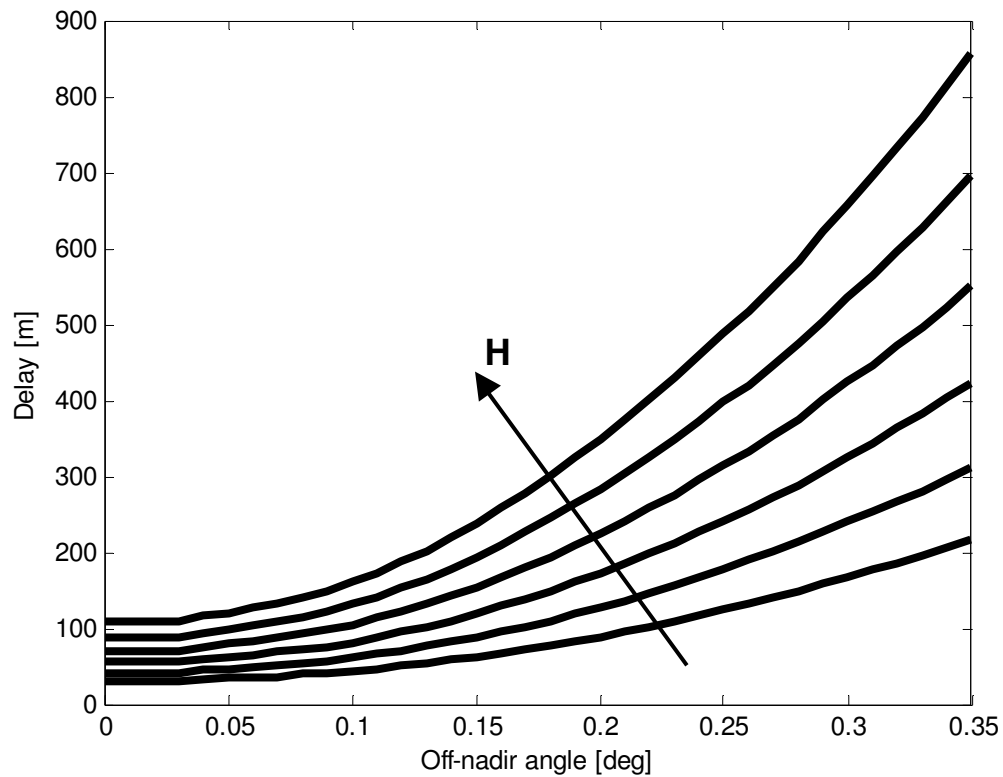


Figure 13 - Delay between waveform centroid and true height evaluated on the basis of developed analytical models, as a function of off-nadir angle and for various spacecraft altitude (H) values (4000 Km up to 9000 Km, step 1000 Km). The corresponding time delay is used for initializing MLE algorithm.

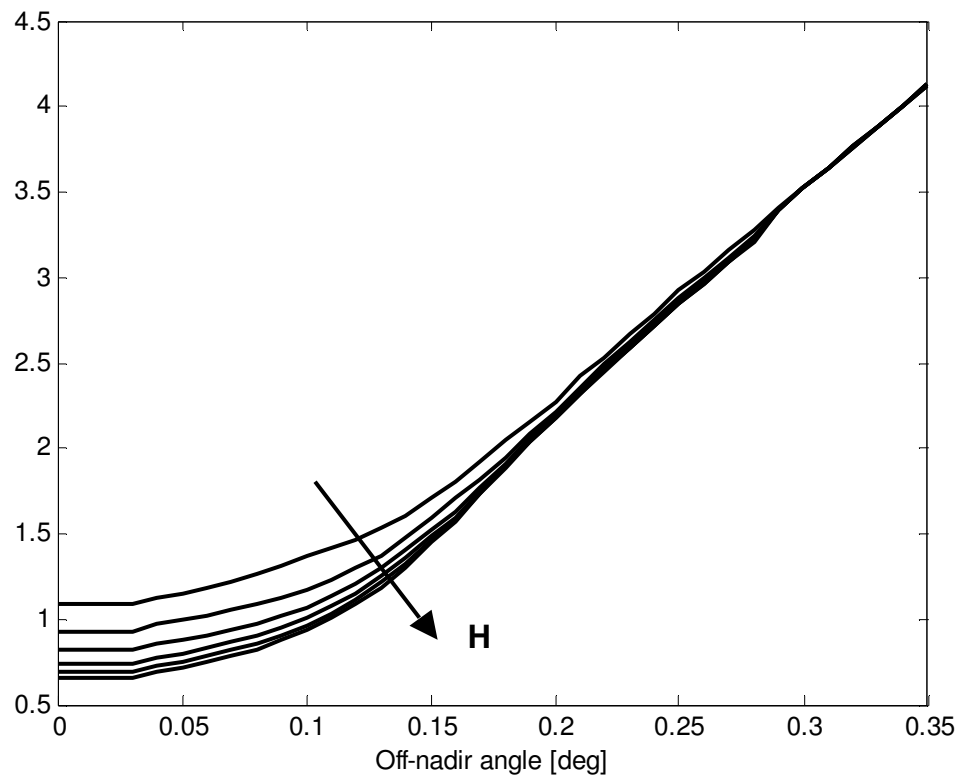


Figure 14 - Model amplitude values for getting a resulting normalized model, as a function of off-nadir angle and for various spacecraft altitude (H) values (4000 Km up to 9000 Km, step 1000 Km).

7 ALGORITHM CORRECTION

The developed model for near-nadir altimeter (Prony's approximation eq. 34) measurements is high dependent on off-nadir angle values. Figure 15 shows some examples of possible model variation caused by changing values of the off-nadir angle. Of course, an increase of the off-nadir angle can imply a significant enlargement of the model.

It is worth noting that, the ξ angle of (34) includes the actual off-nadir angle caused by satellite pointing during fly-by but also a possible mean surface slope of the imaged Titan's area. This effect should be corrected since it influences significantly the final MLE performance.

To this aim, two main parameters characterizing the model's equivalent "width", have been evaluated: the total integral (I) and the standard variation σ , such as:

$$I = \int w(t) dt \quad (48)$$

$$\sigma^2 = \int t^2 w(t) dt - \bar{w}^2$$

$$\bar{w} = \int tw(t) dt \quad (49)$$

Figure 16 and Figure 17 shows the previous parameter as a function of the off-nadir angle and for various radar altitude.

These values of I and (σ) can be used to correct the values of ξ angle of (34) during the MLE algorithm in the following way:

1. each burst is range compressed and the pulses averaged;
2. the two parameters I and σ are evaluated for each averaged waveform;
3. by using the actual radar altitude and off-nadir angle provided by input ancillary data, the correction factor for the ξ angle of near-nadir model can be evaluated from curves of Figure 16 and Figure 17 by using a bi-dimensional spline interpolation.

The obtained correction factor allow either to estimate the local surface slope and to improve the final performance of MLE algorithm.

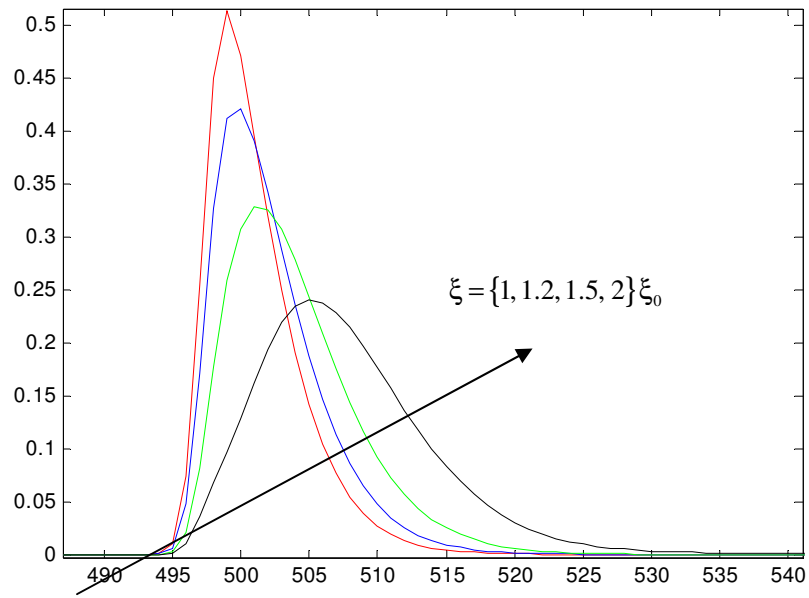


Figure 15 – Altimeter impulse response evaluated by using near-nadir model for various off-nadir angle values

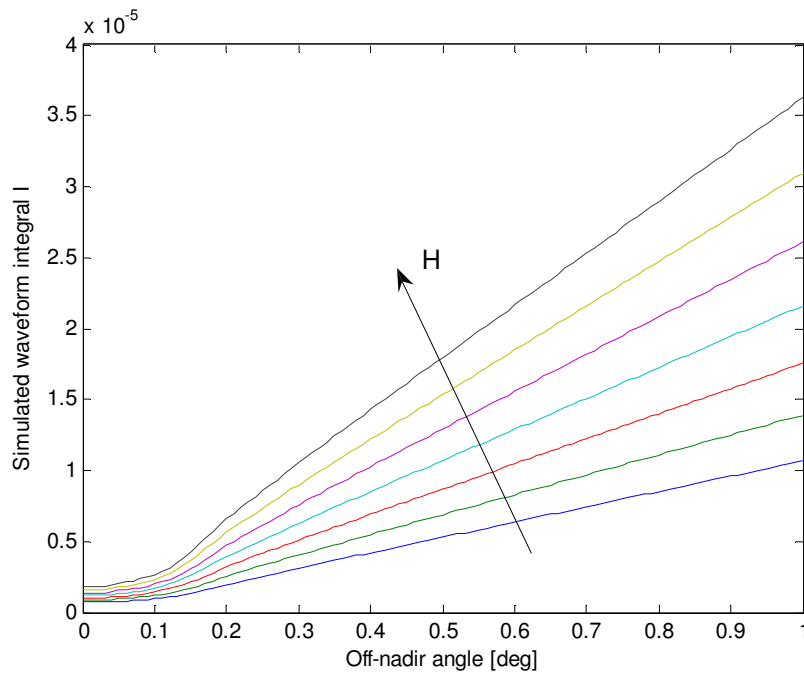


Figure 16 – Model's integral (I) as a function of the off-nadir angle for various radar altitude (H ranging from 6 Km to 12 Km, 1 Km step)

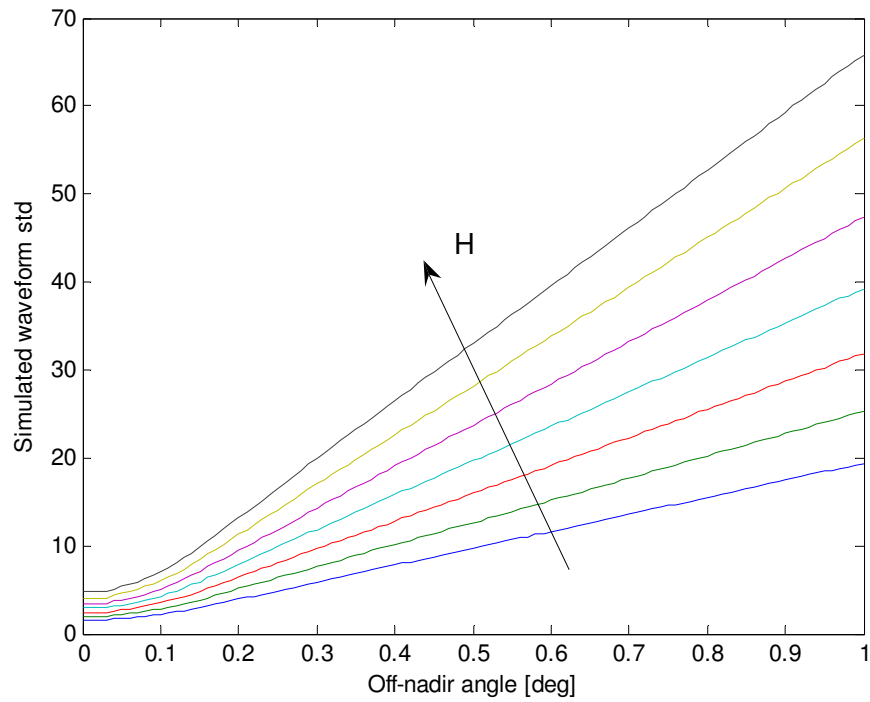


Figure 17 – Model’s standard variation (σ) as a function of the off-nadir angle for various radar altitude (H ranging from 6 Km to 12 Km, 1 Km step)

8 PAD SYSTEM

The algorithms described in the previous paragraphs have been accepted by CASSINI science group and they have been officially used for processing fly-by data and for archiving results in PDS node. En fact, as part of the Cassini Radar Program, ASI is in charge of processing Cassini altimetry data.

This task is performed in the framework of PAD facility, that contains hardware and software tools necessary to receive and elaborate the instrument raw data sets, generate and archive the science data products.

The system is able to manage BODP (Burst Ordered Data Products) files supplied by JPL compliant to PDS (Planetary Data System) standards.

The physical architecture of the PAD System is reported in Figure 18. It is composed by several software components running on two operating system platforms. The first is a server that hosts the local data archive and it is supported by a Linux operating system. The local archive is accessed as a network drive by the data processing subsystem. The second is a client platform where all data processing algorithms are working under Windows® XP Professional operating system.

The core of data processing is represented by a set of algorithms and tools developed in a Matlab® environment. Each tool is provided with a user-friendly graphical interface (GUI), which allows users to exploit all implemented functionalities.

The architectural design of PAD tools is shown in Figure 19, where the following main logical components can be identified:

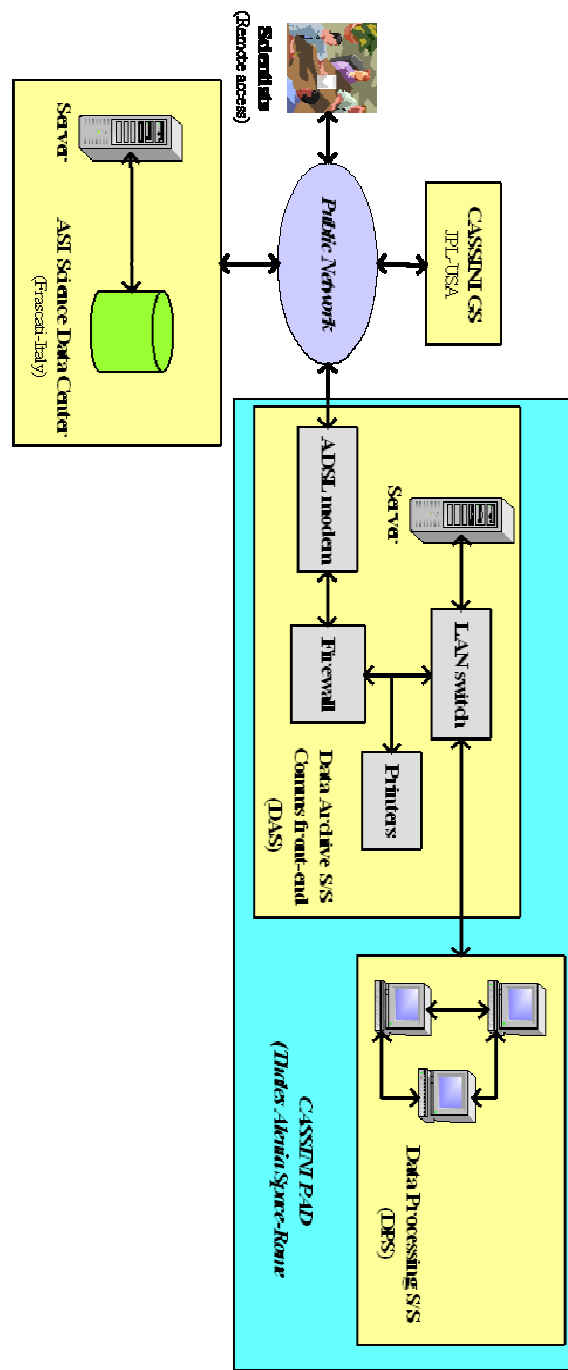


Figure 18 - PAD System Physical Architecture

PAD Framework

The main functionality of the PAD Framework software is to give users a global vision of the status of all the operations that can be made on the BODP files within the Cassini Radar PAD. It provides easy access to all system functionalities. Users can select the flyby to operate and start any operation available for the processing of telemetry files (see Figure 20).

PAD File Manager

The PAD File Manager is the software component that allows users to import the PDS telemetry files into the Local Archive, and to deliver the output ABDR products to the scientific community. The LBDR data retrieval can be executed through the JPL secure HTTPS site, or from any file system location indicated by the user. The delivery functionality can publish the ABDR file on a public FTP repository and/or copy it to a writable portable transfer media.

PAD Data Publisher

The PAD Data Publisher is the software component containing all the commands and the methods that allow users to forward the ABDR files to the Cassini Ground System repository located at JPL. The produced ABDR file is not physically sent nor moved to the Cassini Ground System repository located at JPL. Once the PAD File Manager has published the ABDR files to the public FTP repository, the scientific community receives an e-mail notification to access the password protected repository in order to download the new available file.

ABDR Production Tool

The off-line ABDR Production Tool (PT) retrieves the input LBDR files by managing a list of LBDR files locally stored, allowing user to select the input file (see Figure 21, showing an example of PT GUI). After interactive selection of the LBDR file to be processed, the tool proposes to start the creation of subsets of the input LBDR product (intermediate PT Files) each containing only data records pertinent to one of the active Cassini Radar operational modes, i.e. Altimeter, SAR

and Scatterometer mode. These files are created for internal use and stored into the local archive in both binary and ASCII format, in order to be accessed by SLT.

The PT allows user to perform the generation of the ABDR product starting from the selected LBDR file. Moreover, user is allowed to interactively modify selected keywords into ABDR PDS label.

An ABDR file is produced which contains records for only the two periods (one inbound, one outbound) in which the radar is in altimeter mode, by filling in automatically all the appropriate data fields in the Science Data Segment with the values obtained from SLT processing, and by filling the end of each record in the LBDR file with the values resulting from range compression of sampled echoes data counts (i.e. the altimeter profile), starting from SLT results files. When LBDR processing is terminated, the ABDR PT stores the new file into the local archive along with a report file. Data contained into the ABDR product shall be validated by using SLT functionalities, before submission to the local file server.

Science Look Tool

The off-line Science Look Tool (SLT) is in charge to perform the altimetric processing. It is a graphical application including procedures and algorithms designed to check and simulate the performances of the Cassini Radar Altimeter through calculation, visualization and plotting of relevant parameters (see Figure 22, showing an example of SLT GUI). The SLT uses an intermediate BODP file produced by the ABDR Production Tool, stored into the local archive, and it automatically performs range compression of sampled data.

The SLT evaluates the altimeter profile range start, altimeter profile range step and altimeter profile length required for the PT ABDR production functionality, starting from compressed data. Each compressed burst is typically constituted of 15 chirp pulses. In order to reduce the speckle, a single pulse is obtained by averaging all the received pulses within the burst. Hence, each compressed burst becomes an array containing only one averaged pulse-compressed echo. The averaged bursts are stored

into internal memory as bi-dimensional arrays.

The range compressed data are used to perform waveform analysis and final altitudes estimate by using different altimetry models previously implemented. In addition, the tool permits user to simulate the performances of the Cassini Radar Altimeter, thus allowing obtaining a complete analysis of ALT data from a scientific perspective.

In order to infer the significant geophysical parameters describing the surface's topography from the altimetry data, a Maximum Likelihood Estimator (MLE) has been implemented to be enclosed in the developed algorithm. The Maximum Likelihood Estimator algorithm is based on fitting averaged bursts with a theoretical model describing the Radar Impulse Response. The algorithm is able to select automatically which is the best theoretical model to be used during the processing. The selection is based on threshold criteria related to the current value of the off-nadir angle, in order to cope with the expected occurrence of near-nadir measurements along the hyperbolic trajectory followed during the flyby. All the performances have been numerically evaluated: this method ensures the best fitting of data, thus reducing the errors in heights estimation.

The SLT Tool allows users to specify the default processing parameters by using a Configuration File containing:

- threshold values for off-nadir angles
- minimum number of MLE iterations
- first attempt values
- thresholds for MLE Error Reducing Procedure, etc.

The SLT provides several auxiliary functionalities that allow the user to obtain the complete monitoring of both processing and results. On user request, the SLT provides 2-D or multi-plots of S/C and Radar ancillary data, processing results and algorithm configuration. All the results can be exported (i.e. printed/saved) by user. In addition, on user request, a report file in xml format is generated containing all the

results produced by the SLT, e.g. relevant processing parameters, MLE procedure results, relative elevations of Titan's surface vs. along-track distance (i.e. topographic profiles), altimeter waveforms vs. range bins, ancillary data (e.g. observation geometry and orbital parameters vs. time, instrument data, etc.), surface parameters vs. along-track distance, etc. It will be used by scientists for further validation of data, which is propaedeutical to ABDR production.

Map Tool

The off-line PAD Map Tool (MT) is a graphical application that allows users to visualize and navigate through Titan's 2D and 3D maps, finalized to the analysis of their informative content, as immediate instrument of interpretation of scientific data (see Figure 23, showing an example of MT GUI). From the point of view of scientific surveying, altimetric maps could be confronted and joined with maps obtained by radiometric surveys and with the analysis made by other instruments onboard the Cassini Spacecraft, in order to provide a global vision, as far as it is possible, of the characteristics of Titan's surface.

The purpose of MT is the production of altimetric regional maps obtained by visualization of sub-satellite ground-tracks and overlapping of data collected along tracks to a pre-existent map of Titan, over the region illuminated by the Cassini Radar in high-resolution ALT mode, for each Titan fly-by. Hence, Titan's maps represent the final results of data processing. The realization of the altimetric map can be accomplished by referencing the radar altimetry profile with respect to the surface of Titan.

The Titan's altimetric maps are generated starting from SBDR, LBDR and BIDR data files, and from output data produced by the SLT (e.g. the topographic profile with information about the surface slope, etc.) which could be superimposed to referenced images of Titan surface in a given projection. The content of SBDR, LBDR and BIDR data files is extracted by means of a Data Production Utility, which saves all relevant information needed to produce MT datasets (map internal files)

containing satellite geometry, Scatterometer, Radiometer and SAR data, which becomes then available to Map Tool for visualization.

The SLT output data needed to MT procedures execution are retrieved from the local archive or database. Titan's images (e.g. Mercator albedo maps from HST, ESO, etc, images acquired by optical observation by the Cassini ISS, etc.) to be used as map background, shall be made available, for example by the Cassini Ground System at JPL/NASA, and shall be also stored in the local database. All maps produced by the Map Tool are stored into the local archive, for further distribution.

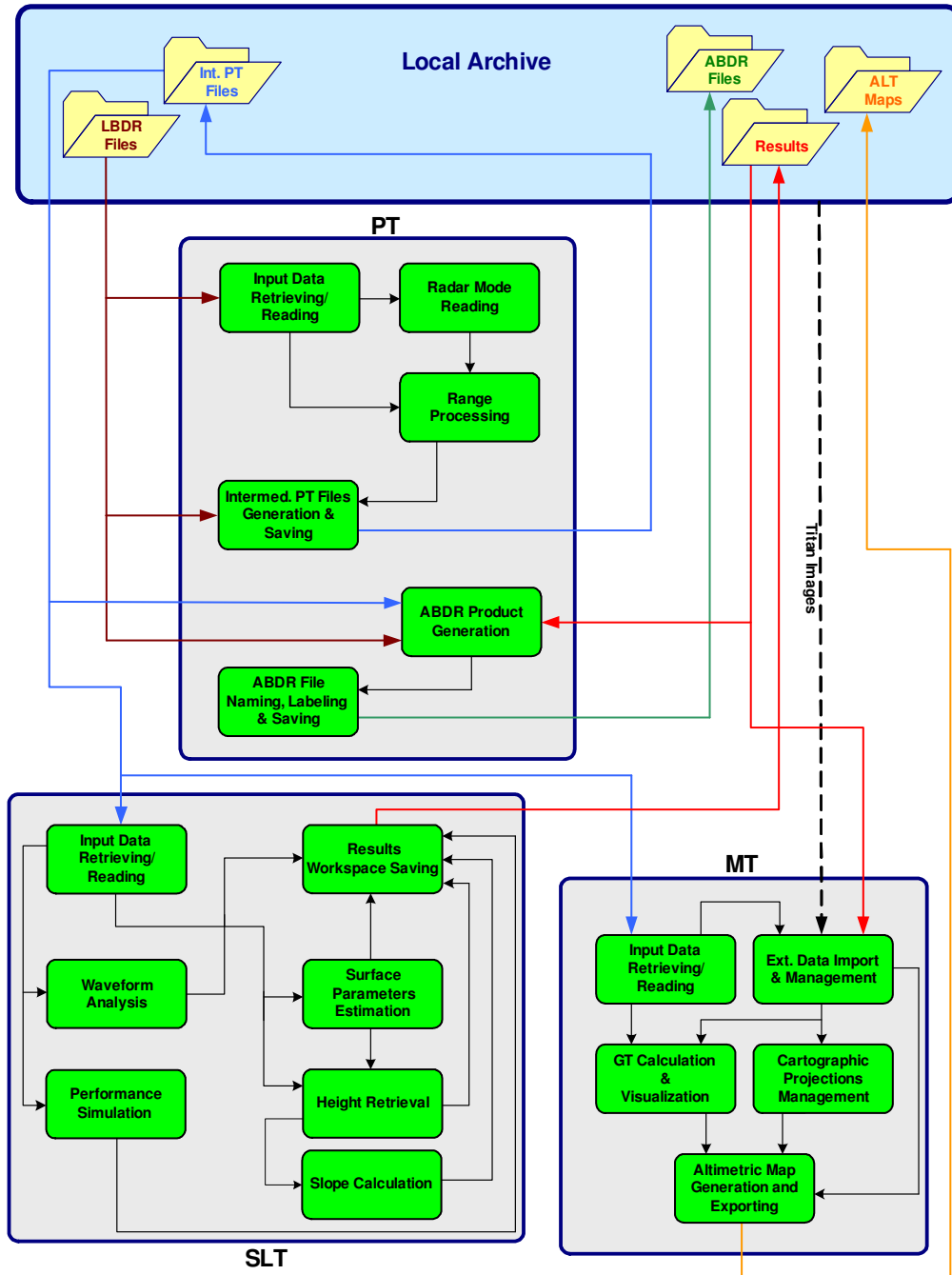


Figure 19 - PAD Tools Architectural Design

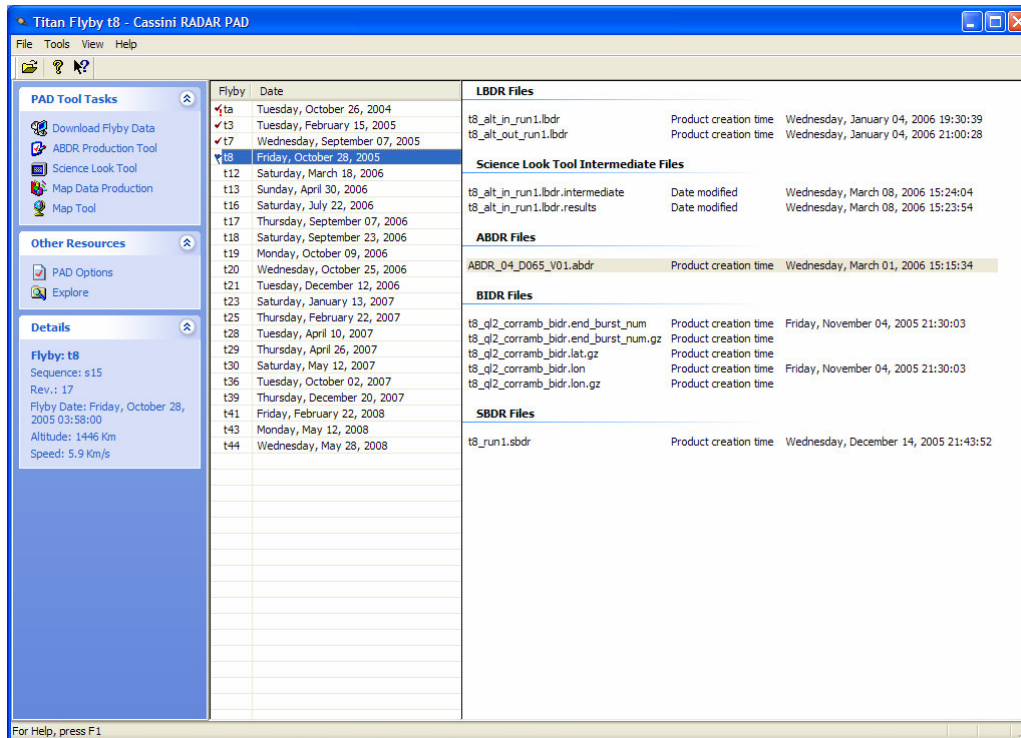


Figure 20 – The PAD Framework

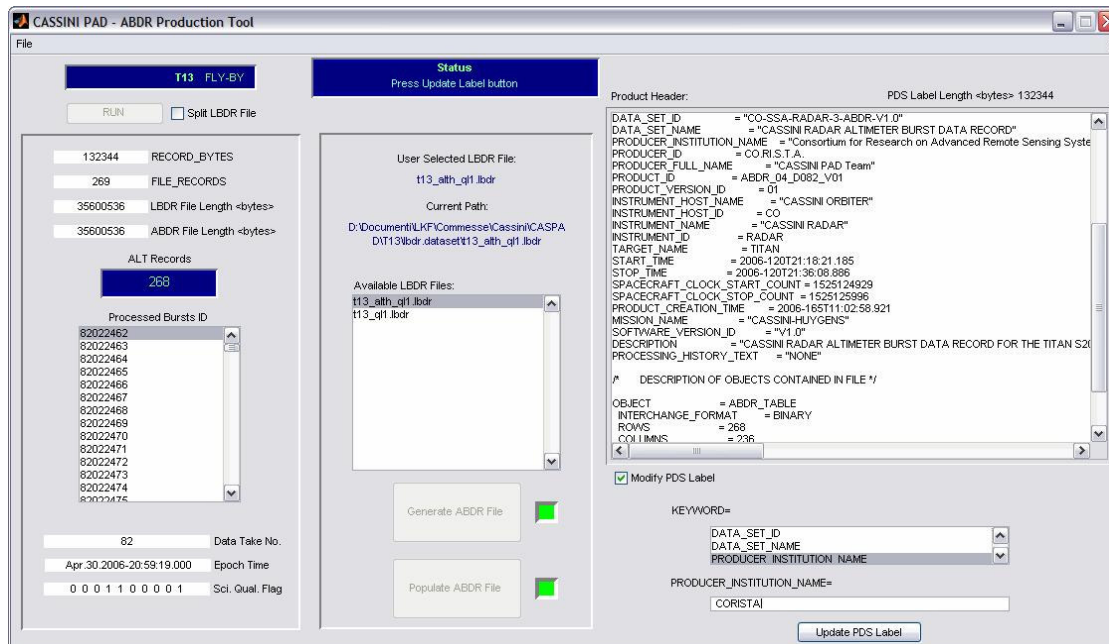


Figure 21 – The Production Tool HMI

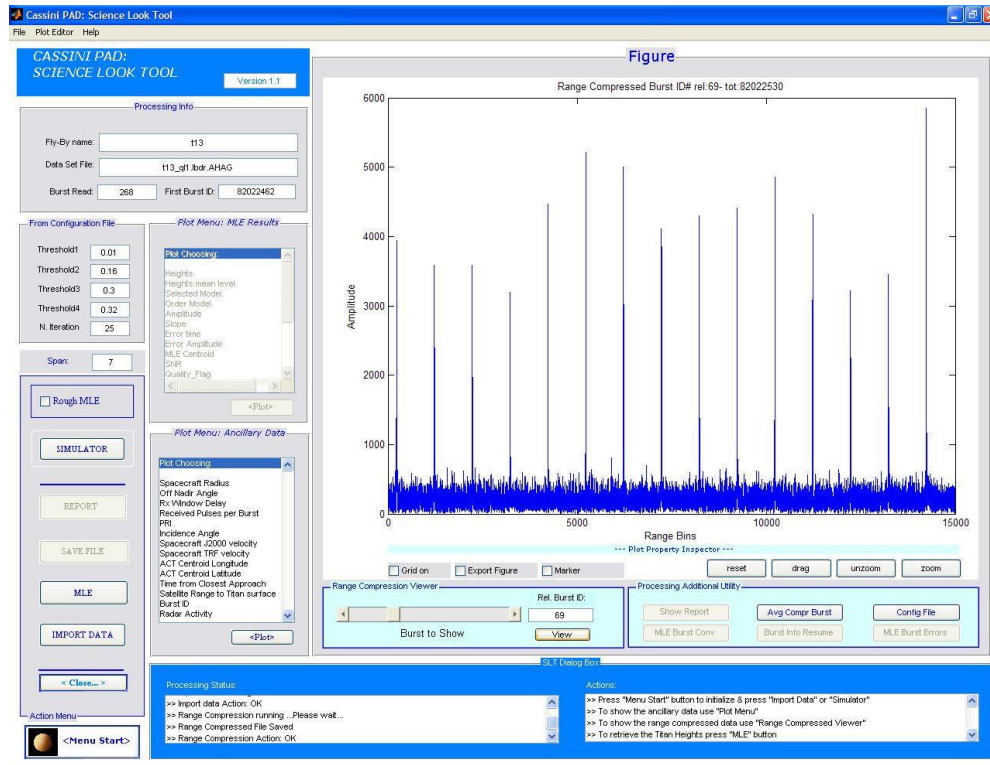


Figure 22 – The Science Look Tool HMI

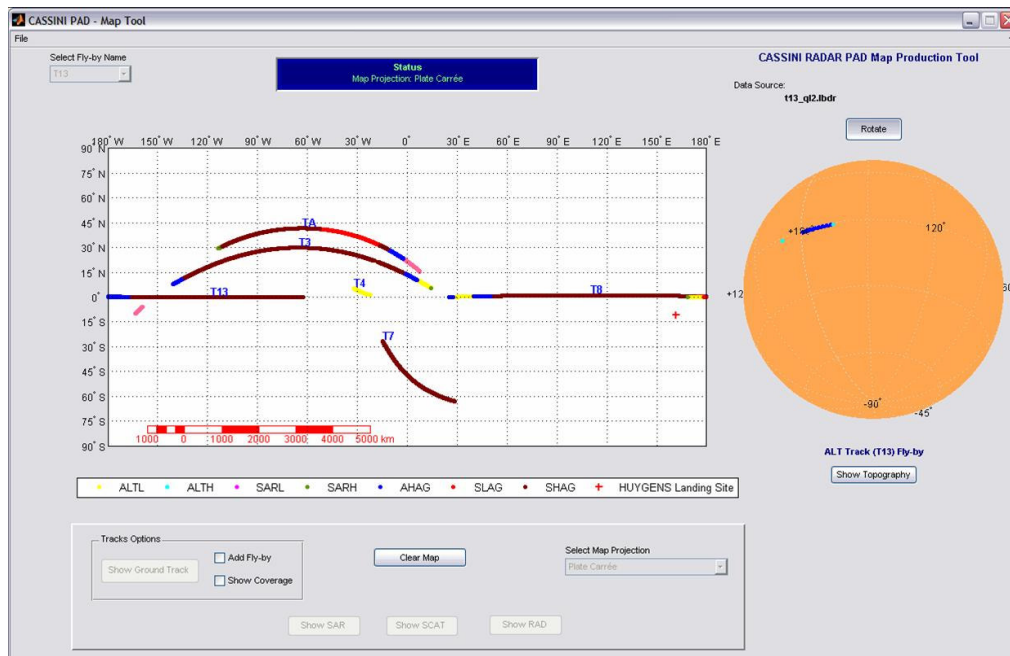


Figure 23 – The Map Tool HMI

9 PROCESSING RESULTS

In this paragraph, some results obtained by using MLE algorithm in the framework of PAD system, are presented. In particular, data processing results of the first operative 11 Titan's fly-bys are taken into account, including the first one done for testing purposes (Ta).

Measurements were also made by the spacecraft on the T7 fly-by in September 2005, but the data were lost due to an on-board recorder anomaly. In Table 5 are summarized the main statistical parameters of the retrieved topographic information. Figure 24, Figure 25, Figure 26 and Figure 27 shows the topographic profiles obtained by processing the all the available fly-bys, where the Titan's height are referred to the mean planet radius of 2575 Km.

It is worth noting that the processing takes also into account the delay due to internal path followed by the transmitted and received signals. This time delay has been evaluated by processing calibration data (rerouted chirp and leakage signal) and it has been found equal to 6 μ sec..

The slope values have been evaluated by taking a linear fit of the height profiles, of course considering the in-bound and out-bound part of the trajectory separately and it has been included for statistical purposes only.

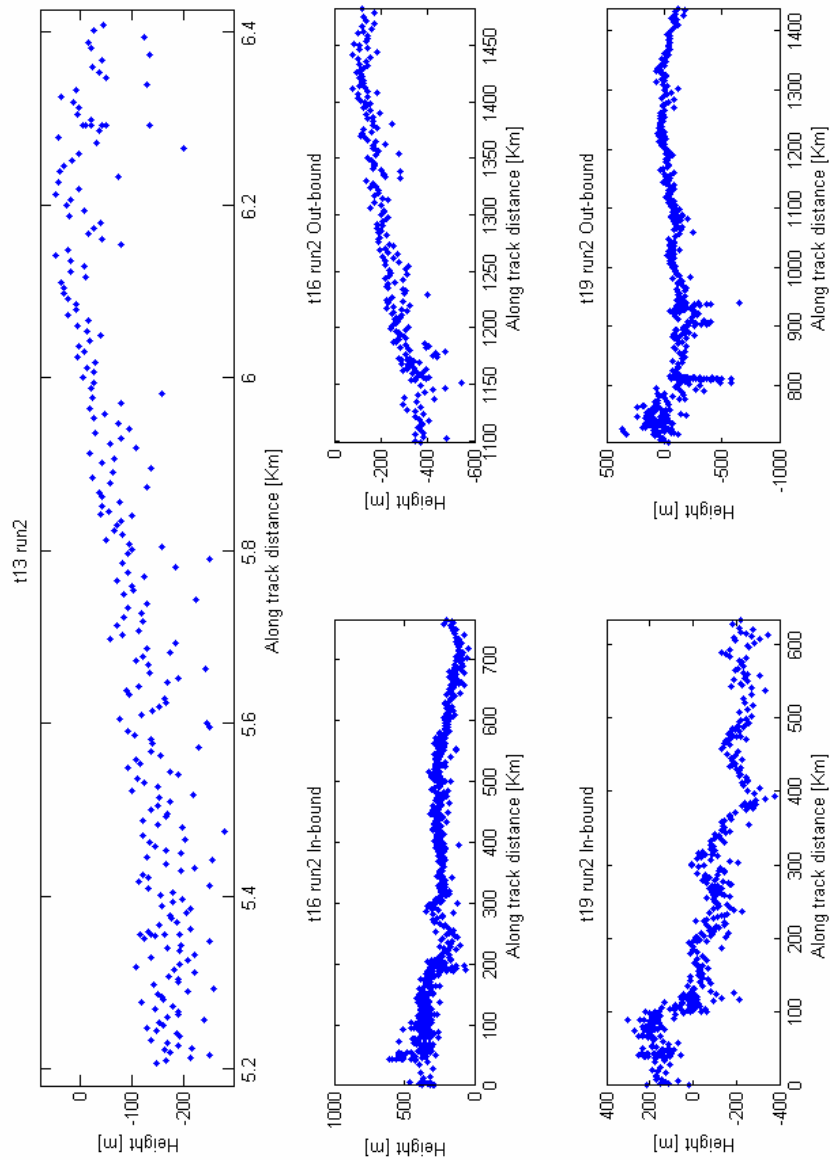


Figure 24 - Retrieved Titan's surface height as a function of along track distance. The height values are referred to Titan's mean radius of 2575 Km (fly-bys T13, T16 and T19). The distance values are referred to altimetric acquisition start.

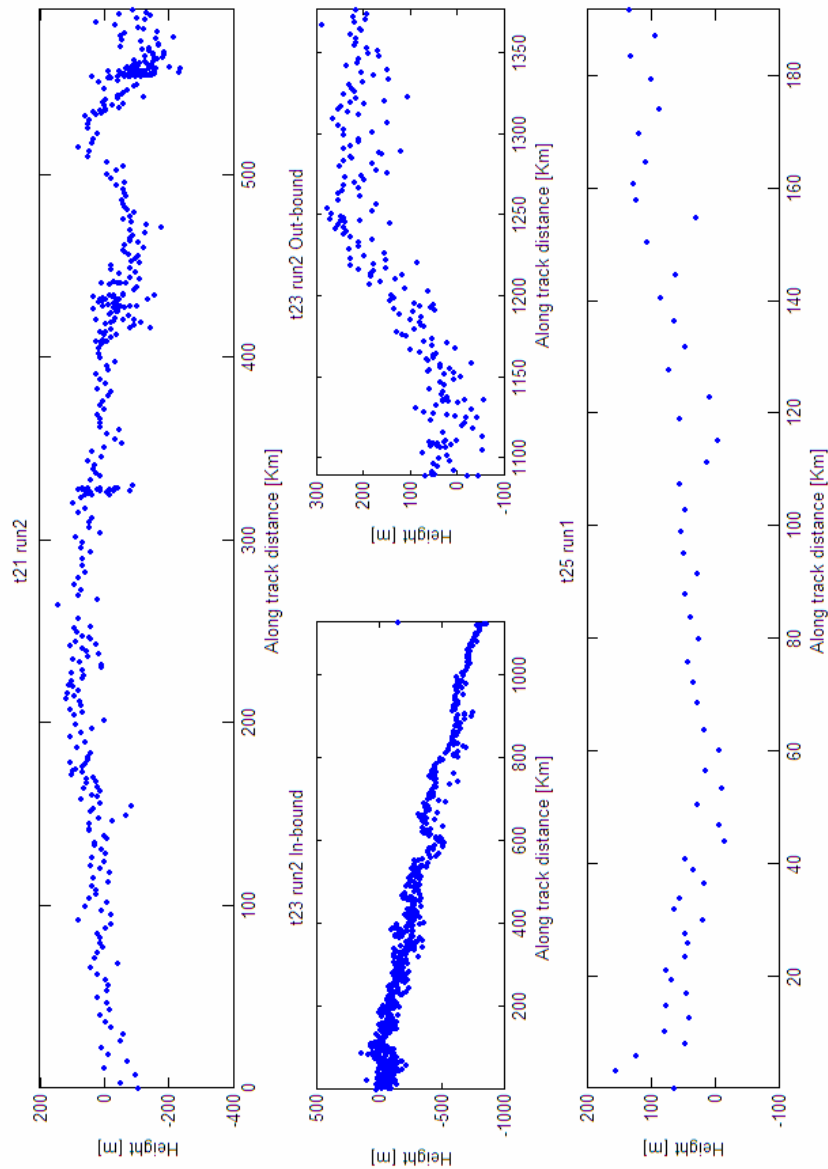


Figure 25 - Retrieved Titan's surface height as a function of along track distance. The height values are referred to Titan's mean radius of 2575 Km (fly-bys T21, T23 and T25). The distance values are referred to altimetric acquisition start.

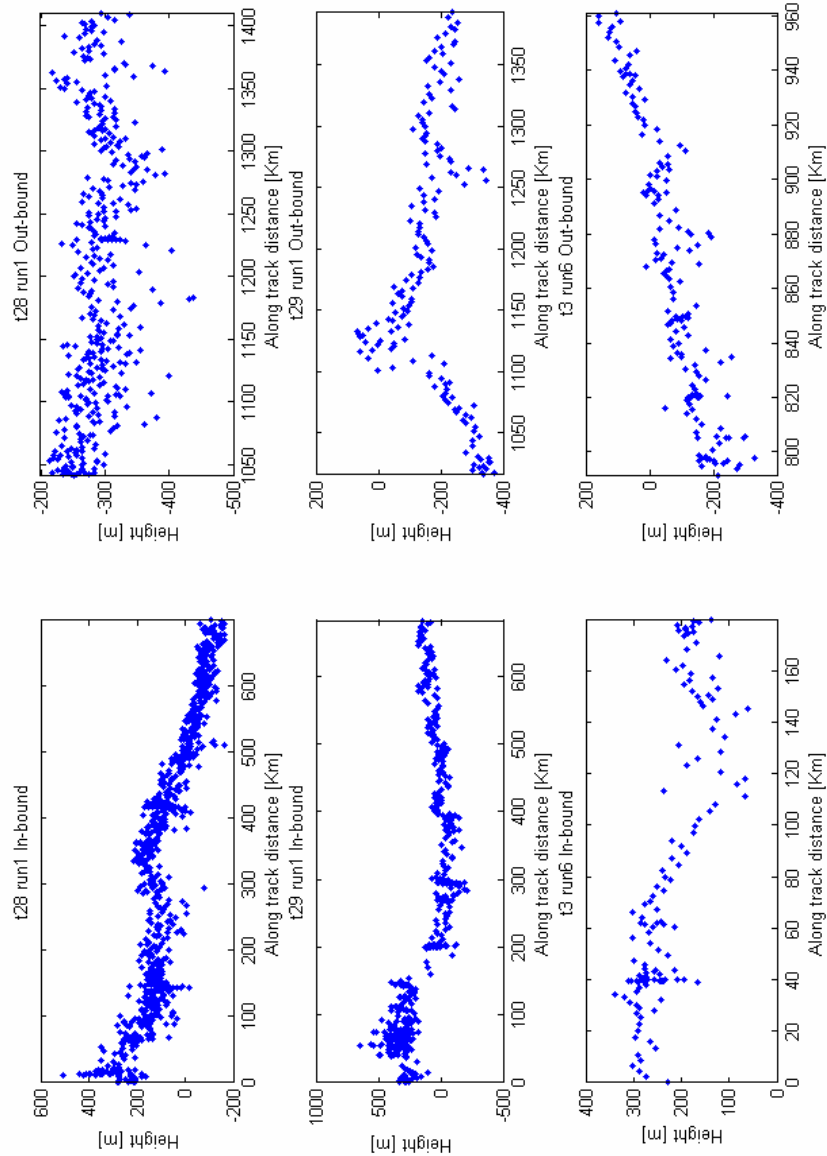


Figure 26 - Retrieved Titan's surface height as a function of along track distance. The height values are referred to Titan's mean radius of 2575 Km (fly-bys T28, T29 and T3). The distance values are referred to altimetric acquisition start.

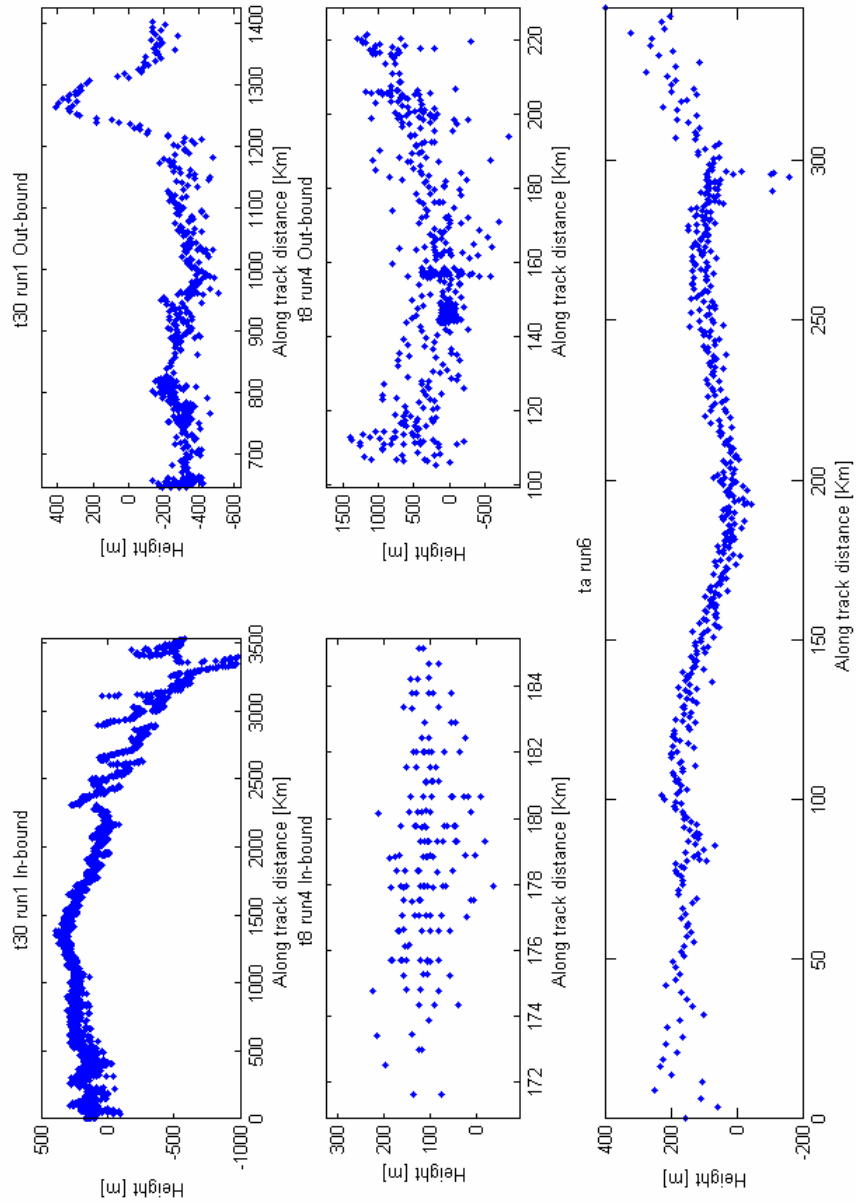


Figure 27 - Retrieved Titan's surface height as a function of along track distance. The height values are referred to Titan's mean radius of 2575 Km (fly-bys T30, T8 and Ta). The distance values are referred to altimetric acquisition start.

Pass	Version	Date	No. of samples	Latitude [°] (start/stop)	Longitude [°] (start/stop)	Height [m]			Slope [m/Km]	
						Min.	Max.	Mean		
Ta	run 6	2004-10-26	458	29.59/22.74	-9.73/-1.51	-158	397	99	65	-0.2
T3-in	run 6	2005-02-15	129	7.91/11.73	-140.61/-133.81	60	338	225	63	-0.9
T3-out	run 6		162	14.72/11.03	-2.83/5.91	-330	159	-75	104	1.9
T8-in	run 4	2005-10-28	165	-3.61/0.14	-178.07/178.51	-708	276	102	82	2.1
T8-out			577	-0.79/0.13	51.06/24.92	-840	1398	254	362	3.2
T13	run 2	2006-04-30	268	-0.04/-1.51	-165.63/178.21	-280	48	-106	79	2.0
T16-in	run 2	2006-07-21	648	12.20/29.18	-154.73/-155.84	42	607	270	91	-0.3
T16-out			238	20.77/12.23	25.27/24.77	-543	-79	-245	97	0.8
T19-in	run 2	2006-10-09	432	32.74/46.38	-140.80/-135.43	-376	301	-47	155	-0.8
T19-out			479	-1.00/-17.35	29.30/32.55	-656	362	-87	135	0.1
T21	run 2	2006-12-12	444	-14.45/-27.31	57.04/49.23	-237	142	-22	73	-0.3
T23-in	run 2	2007-01-13	685	53.56/62.63	-119.58/-91.89	-861	141	-241	217	-0.7
T23-out			202	-28.01/-34.85	33.24/37.74	-57	288	126	93	0.9
T25	run 1	2007-02-22	57	-35.00/-30.8	-39.50/-38.13	-17	155	55	40	0.3
T28-in	run 1	2007-04-10	853	-26.49/-11.04	-33.30/-27.96	-166	507	83	117	-0.5
T28-out			395	55.07/48.29	125.63/133.19	-437	-213	-291	37	-0.1
T29-in	run 1	2007-04-26	490	-19.26/-4.09	-28.98/-25.24	-209	646	137	167	-0.5
T29-out			161	-49.42/41.44	137.06/141.93	-373	67	-170	101	0.1
T30-in	run 1	2007-05-12	2873	-11.16/68.57	-27.63/1.14	-983	388	99	242	-0.2
T30-out			566	68.62/25.55	1.22/147.82	-889	413	-296	177	-0.1

Table 5 - Main statistical information of the 11 fly-bys with available high resolution altimetric data. The slope values are evaluated separately for in-bound (in) and out-bound (out) part of the trajectory.

10 SIMULATION

The final part of the present PhD activities have been dedicated to altimetry echo waveform simulation. The main reason for this effort is to better understand the Titan's surface characteristics by analyzing the signals received by CASSINI radar in altimetric mode.

The approach followed is based on a fractal characterization of Titan's surface, since it is by now widely recognized (see [19], [20], [21]) that fractal models are very useful in the description of natural surfaces because they properly account for the scale invariance property typical of such surfaces.

As Mandelbrot argued [19], classical parameters usually employed to describe natural surfaces (i.e., standard deviation and correlation length) change when the scale at which the surface is observed changes. Conversely, fractal parameters of a natural surface are independent of the observation scale. The most useful fractal model for natural surfaces is the fractional Brownian motion (fBm) [22], [23]. It is a stochastic nonstationary process described in terms of the probability function of its increments, whose sample functions are everywhere continuous, but everywhere nondifferentiable.

A stochastic process $z(x, y)$ is an fBm surface if, for every (x, y, x', y') , it satisfies the following relationship:

$$\Pr\{z(x, y) - z(x', y') < \bar{\zeta}\} = \frac{1}{\sqrt{2\pi s\tau^H}} \int_{-\infty}^{\bar{\zeta}} \exp\left(-\frac{\zeta^2}{2s^2\tau^{2H}}\right) d\zeta \quad (50)$$

where τ is the distance between the points (x, y) and (x', y') .

Pr stands for “probability” and the two parameters that control the fBm behavior are:

- H, the Hurst coefficient ($0 < H < 1$), related to the fractal dimension D by means of the relationship $D = 3 - H$,
- s, the standard deviation of surface increments at unitary distance, a real parameter related to an fBm characteristic length, the topography T, by means of the relationship:

$$s = T^{(1-H)} \quad (51)$$

It has been demonstrated [21], [23], [24] that the spectrum $S(k)$ of an isotropic fBm process is a power law

$$S(k) = S_0 k^{-\alpha} \quad (52)$$

where the spectral and spatial domain parameters are related by the following relationships:

$$\begin{aligned} \alpha &= 2 + 2H \\ S_0 &= s^2 2^{2H} 2\pi H \frac{\Gamma(1+H)}{\Gamma(1-H)} \end{aligned} \quad (53)$$

Γ being the Gamma function. A fractal surface has the property of self-affinity for every scaling factor r, that means:

$$z(rx, ry) = r^H z(x, y) \quad (54)$$

where the equal sign stands for “has the same statistics as”.

Starting from the previous definition, the procedure adopted for generating a fBm surfaces, with spacing Δ , starting from H and T values is based on the following steps:

1. generation of a random matrix of Gaussian distributed independent values;
2. evaluation of the power spectral density following the (52), by using input H and T values;
3. filtering data of step 1 with the power spectral density of step 2;
4. multiplication of data with the scaling factor Δ^H .

An example of possible results is shown in Figure 28, where all negative values have been set to zero for simulating presence of liquid materials.

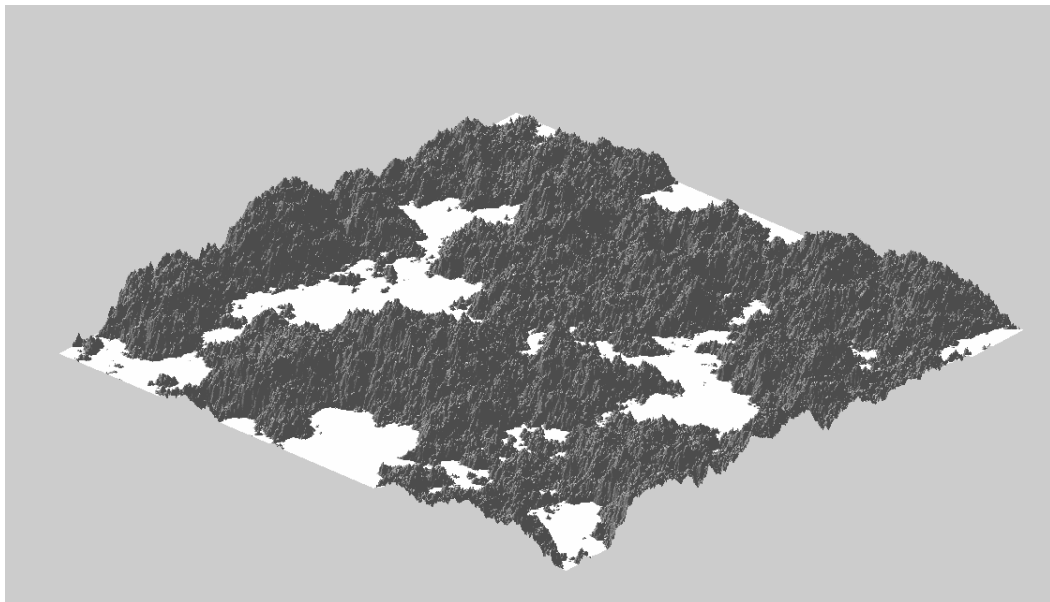


Figure 28 – Fractal surface generated with H=0.65 and T=0.005. All negative values have been set to zero for simulating presence of liquid materials.

Another advantage of the fBm description is related to the analytical evaluation of electromagnetic scattering. In fact, power law spectra are not easy to analytically handle within the Kirchhoff approach and numerical methods and/or Monte Carlo simulations are usually employed to evaluate the normalized radar cross section of a power law surface.

In [25], for the fBm model, the mean-square value of the field scattered along an arbitrary direction by a surface illuminated by a plane wave is evaluated in a closed form, within the Kirchhoff approach and the small-slope approximation. Expression of the backscattering coefficient, i.e., of the normalized radar cross section, is also provided in [25].

This analytical expression has been used for CASSINI radar waveform simulation, such as:

$$\sigma_{hv}^0 = \frac{4\pi R_0^2 \langle |E_v^{(s)}|^2 \rangle}{A |E_h^{(i)}|^2} \quad (55)$$

where:

h and v stands for horizontal or vertical polarization

R_0 is the distance from the target

$E_h^{(i)}$ is the incidence field

$E_v^{(s)}$ is the scattered field

A is a constant

The scattered field can be expressed as function of the incidence field as follow:

$$\langle |E_v^{(s)}|^2 \rangle = \frac{k^2 |E_h^{(i)}|^2 |F_{hv}|^2}{(4\pi R_0)^2} 2\pi A \int_0^\infty J_0(v_x \tau) \exp\left(-\frac{1}{2} v_z^2 s^2 \tau^{2H}\right) \tau d\tau \quad (56)$$

where:

$$k = \frac{2\pi}{\lambda}$$

F_{hv} is related to the Fresnel R coefficient as follow:

$$\begin{aligned} F_{hh}(\vartheta) &= -2R_h(\vartheta) \cos(\vartheta) \\ F_{hv}(\vartheta) &= F_{vh}(\vartheta) = 0 \\ F_{vv}(\vartheta) &= -2R_v(\vartheta) \cos(\vartheta) \end{aligned} \quad (57)$$

J_0 is the zero order Bessel Function

$$\begin{aligned} v_x &= 2k \sin(\vartheta) \\ v_z &= -2k \cos(\vartheta) \end{aligned} \quad (58)$$

and

$$R_h = \frac{\cos(\vartheta) \sqrt{\varepsilon} - \sqrt{1 - \frac{\sin^2(\vartheta)}{\varepsilon}}}{\cos(\vartheta) \sqrt{\varepsilon} + \sqrt{1 - \frac{\sin^2(\vartheta)}{\varepsilon}}} \quad (59)$$

$$R_v = \frac{\cos(\vartheta) - \sqrt{\varepsilon - \sin^2(\vartheta)}}{\cos(\vartheta) + \sqrt{\varepsilon - \sin^2(\vartheta)}} \quad (60)$$

ε is the relative dielectric constant of actual terrain

Therefore, the backscattering coefficient can be written as:

$$\sigma_{hv}^0(\vartheta) = k^2 |F_{hv}|^2 \int_0^{\infty} J_0(2k \sin(\vartheta) \tau) \exp(-2k^2 \cos^2(\vartheta) s^2 \tau^{2H}) \tau d\tau \quad (61)$$

Figure 29 and Figure 30 show some examples of backscattering coefficient for CASSINI radar evaluated by using the last relationship for various H and T values.

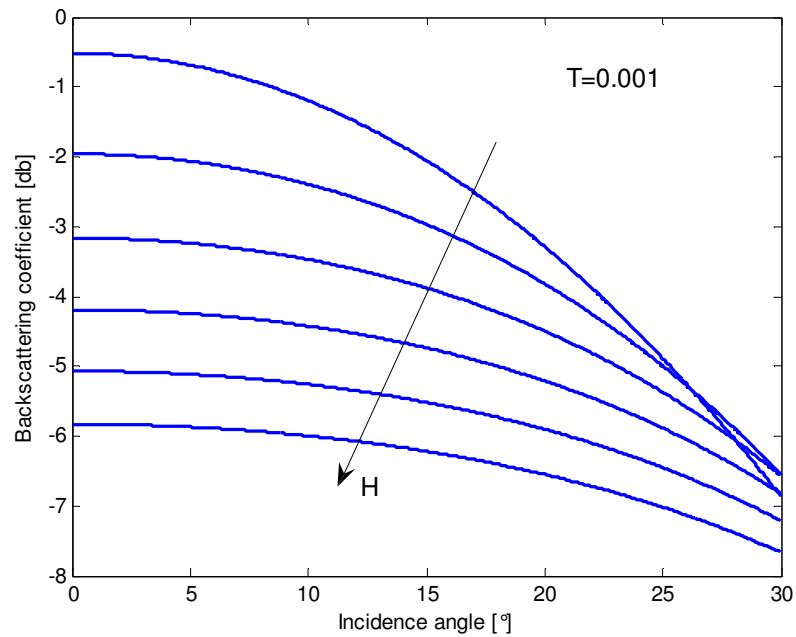


Figure 29 – Backscattering coefficient for CASSINI radar as a function of the incidence angle for various H values (H from 0.6 to 0.85, step 0.05)

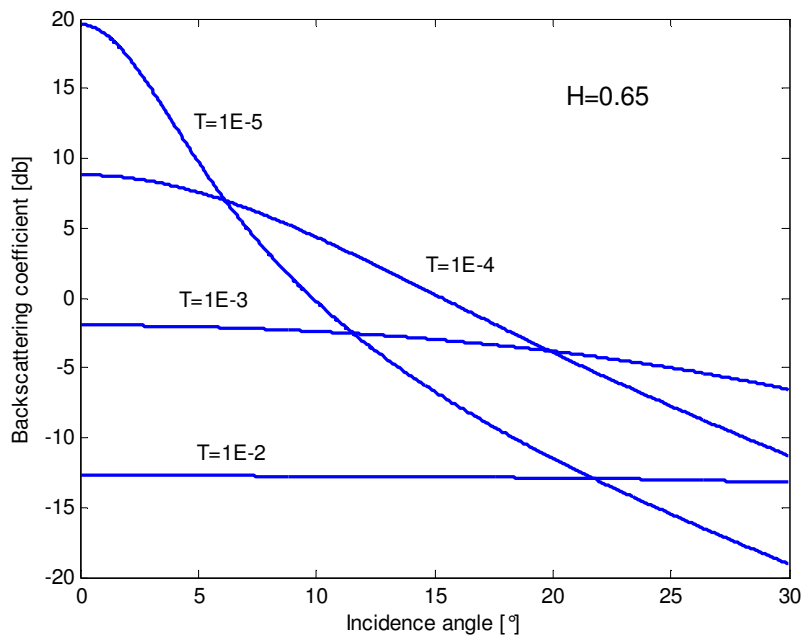


Figure 30 – Backscattering coefficient for CASSINI radar as a function of the incidence angle for various T values

Having fixed the model for surface statistical characterisation and the related back scattering coefficient, algorithm for simulating CASSINI radar received power echoes can follow the scheme of Figure 31. The following main steps can be identified:

- Given H and T values, a surface is generated as fBm process. The simulated area extent is chosen taking into account the actual CASSINI antenna footprint (e.g. 3 times the antenna footprint, about $130 \times 130 \text{ Km}^2$ at 6000 Km of radar altitude). The surface pixel size is related to horizontal radar resolution (e.g. 1/5 of horizontal resolution, about $4 \times 4 \text{ Km}^2$ at 6000 Km of radar altitude).
- Local slope is evaluated with a bi-dimensional algorithm and, consequently, the incidence angle can be assessed with respect actual radar position.
- The backscattering coefficient is evaluated for each facet, according to the surface incidence angle and weighted by antenna pattern. Actual CASSINI satellite attitude is taken into account.
- Received power echoes is evaluated by coherently superimposing all contributions coming from single surface facets, taking into account radar equation and time delay.

Figure 32 shows some examples of simulated waveforms that should be averaged in order to obtain the final mean echo.

The shape of the mean radar echo depends on fractal parameters (H and T) but also on radar ancillary data, such as altitude and off-nadir angle.

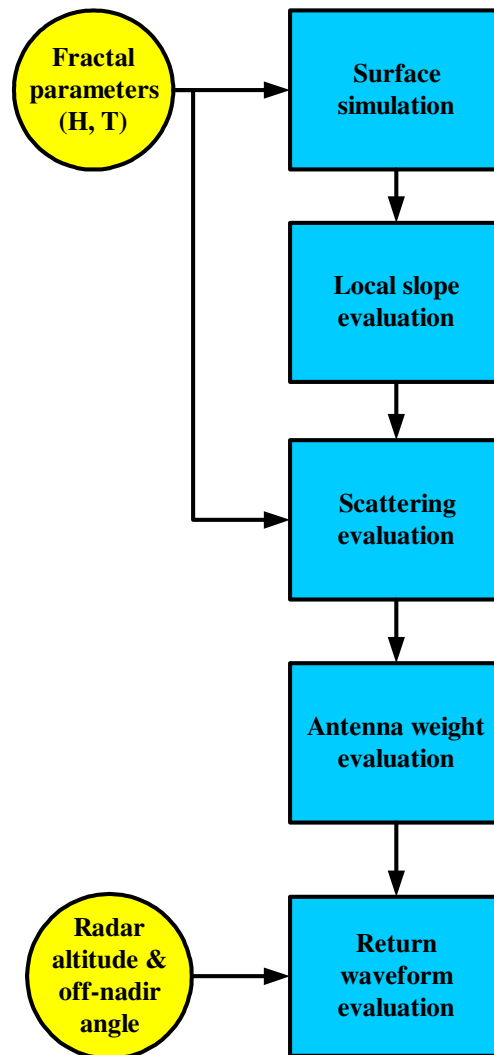


Figure 31 – Algorithm used for simulating CASSINI radar received power echoes

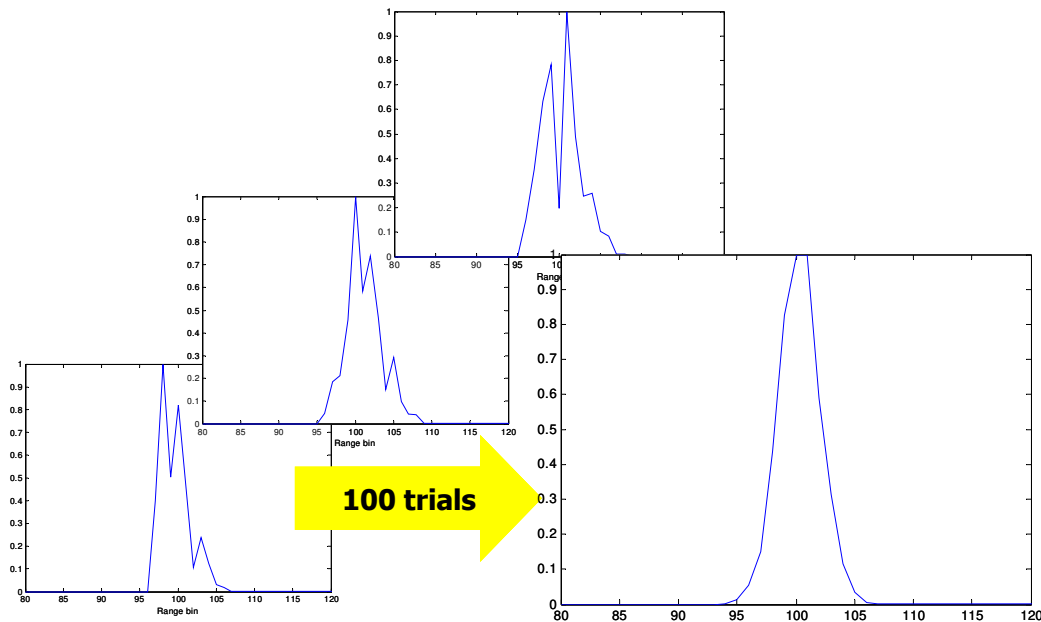


Figure 32 – Examples of simulated CASSINI radar waveforms and the resulting averaging

To better understand these dependencies, various simulations have been performed according to the following scheme:

- H from 0.5 up to 0.66, with 9 values
- T from $0.005/k$ up to $0.1/k$, with 6 values), being $k=2\pi/\lambda$
- Altitude from 4000 Km up to 10000 Km, with 7 values
- off-nadir angle from 0° up to 0.5° , with 11 values

For each mean simulated echo, some statistical parameters have been evaluated: I, II moment and skewness. The results are reported in Figure 33, Figure 34 and Figure 35.

A quick analysis of these figures shows that only II moment and skewness are strongly dependent on fractal parameters, while I moment is mainly related to radar altitude and off-nadir angle.

These curves can be used to infer fractal parameter from actual altimetric data, by using ancillary information and by interpolating the evaluated values of II moment and skewness.

A preliminary attempt to use this procedure for estimating fractal parameters of Titan's surface has been done by using data of T30 fly-by. The analysis has been limited to those burst where radar altitude was in the range 4000-10000 Km. Figure 36 shows the selected zone on the whole radargram of the fly-by.

Figure 37 shows a comparison between measured values of II moment and skewness and interpolated ones, while Figure 38 shows the final results for H and T.

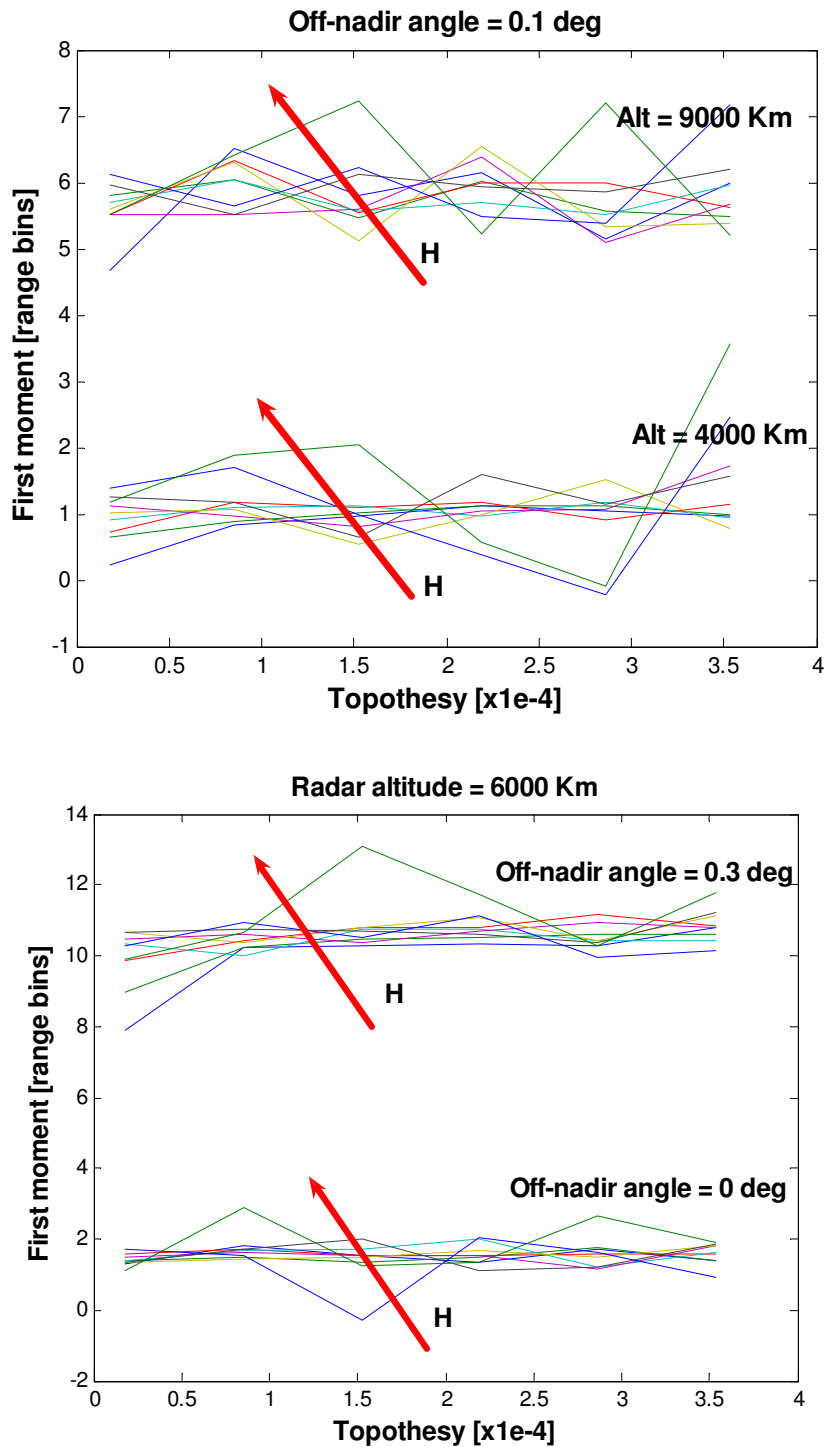


Figure 33 – Simulated waveform: I moment as a function of Topothesy for various radar altitude, Hurst coefficient and off-nadir angle values

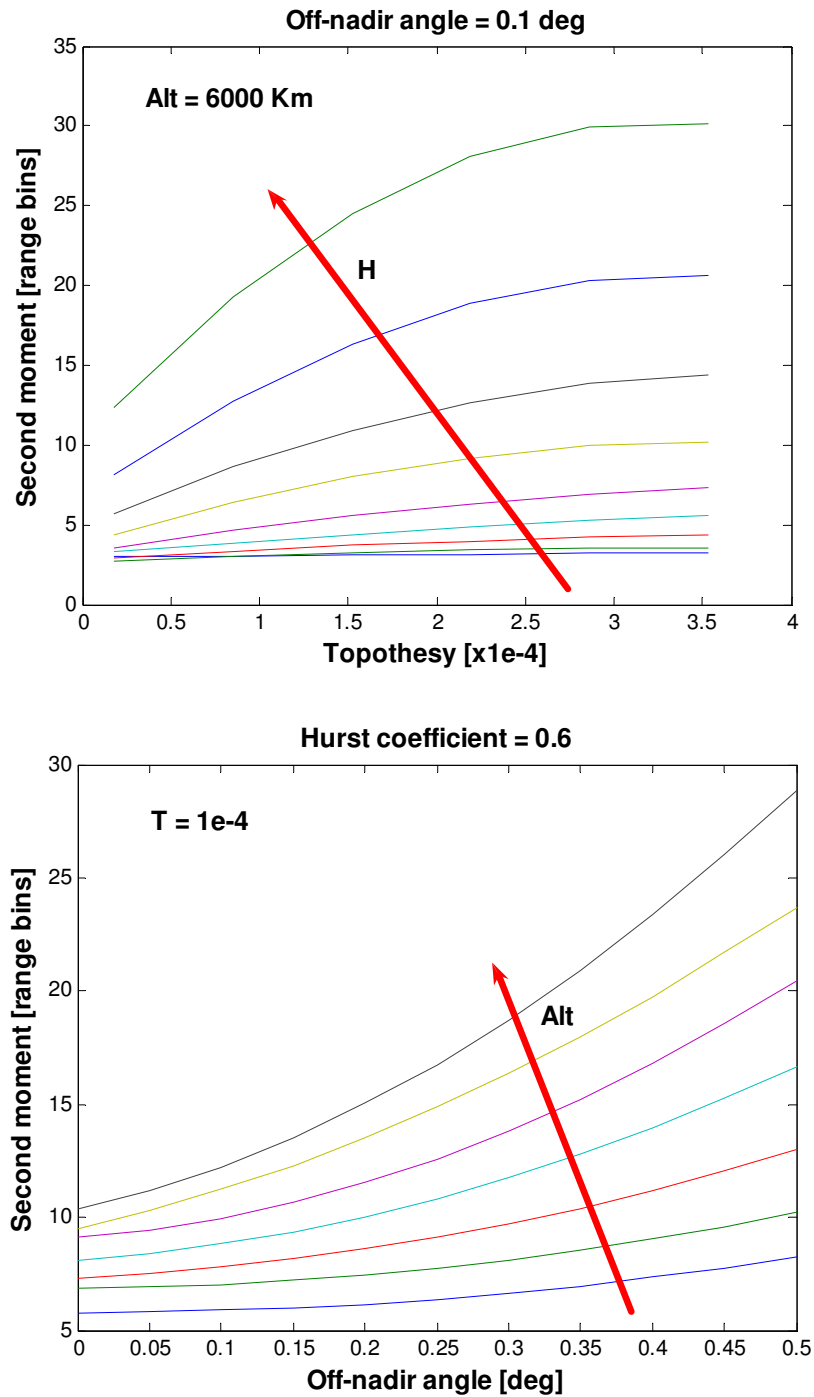


Figure 34 – Simulated waveform: II moment as a function of Topothesy (upper figure) and off-nadir angle (lower figure) for various radar altitude, Hurst coefficient and off-nadir angle values

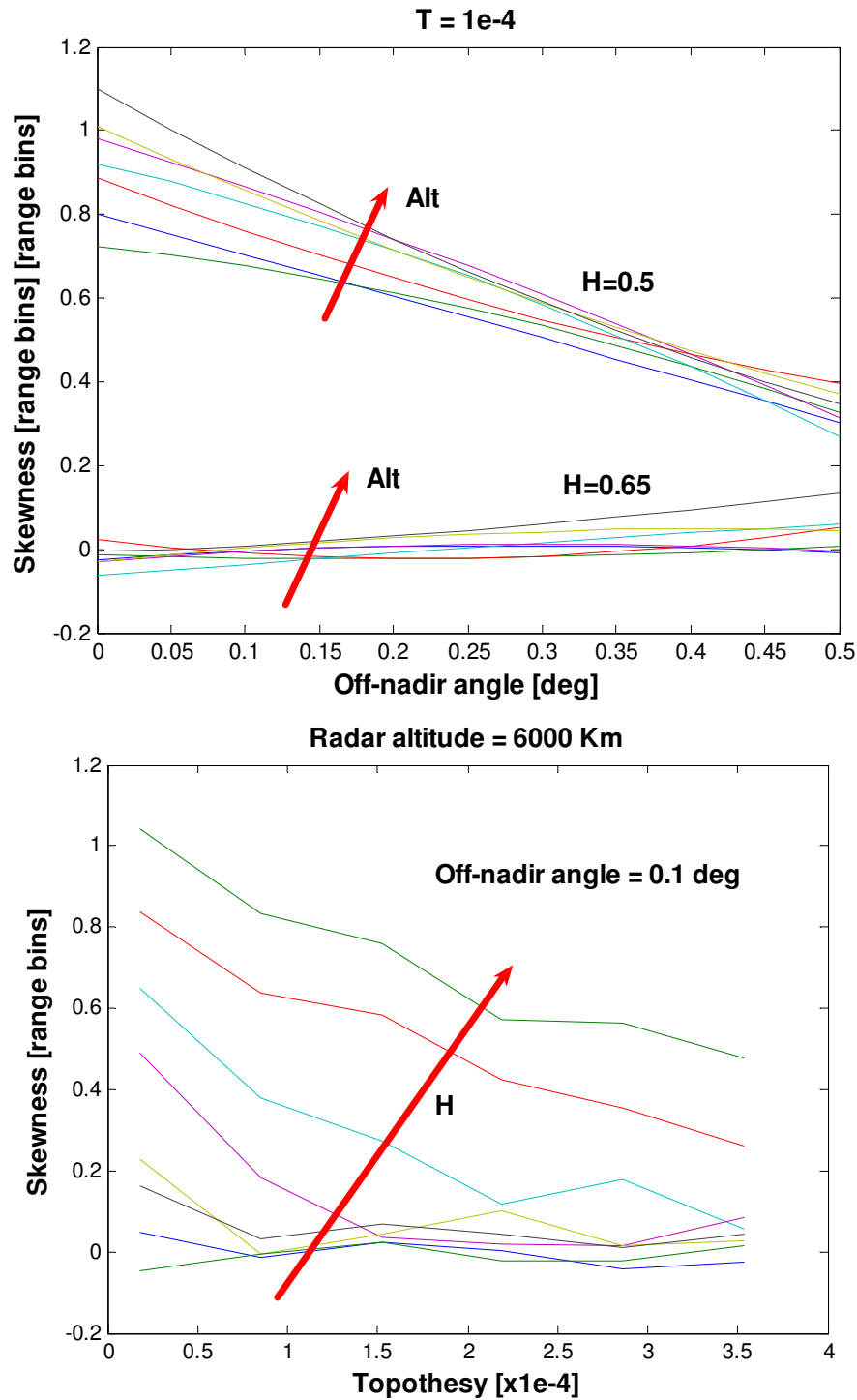


Figure 35 – Simulated waveform: skewness moment as a function of Topothesis (lower figure) and off-nadir angle (upper figure) for various radar altitude, Hurst coefficient and off-nadir angle values

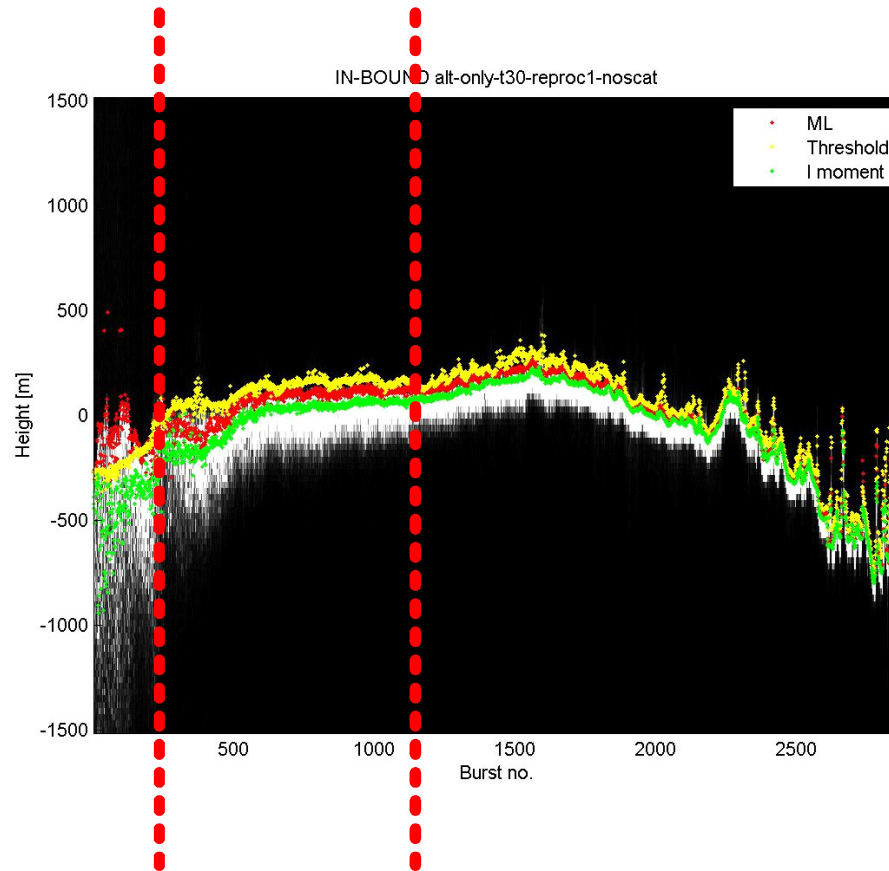


Figure 36 – Radargram of T30 fly-by: the two dotted red lined limit the zone where the procedure for estimating the fractal parameters of the surface has been applied

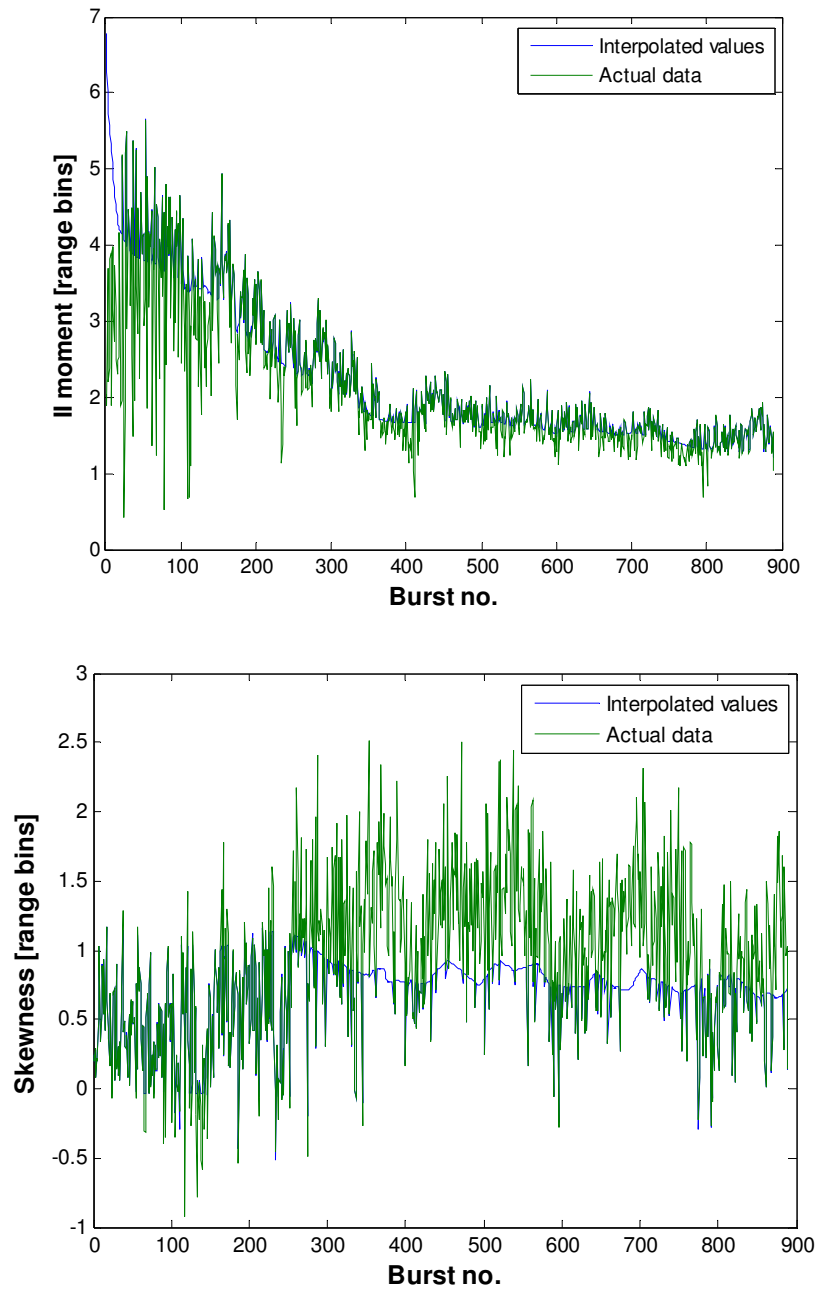


Figure 37 – Results of the procedure for estimating the fractal parameters applied to T30 fly-by

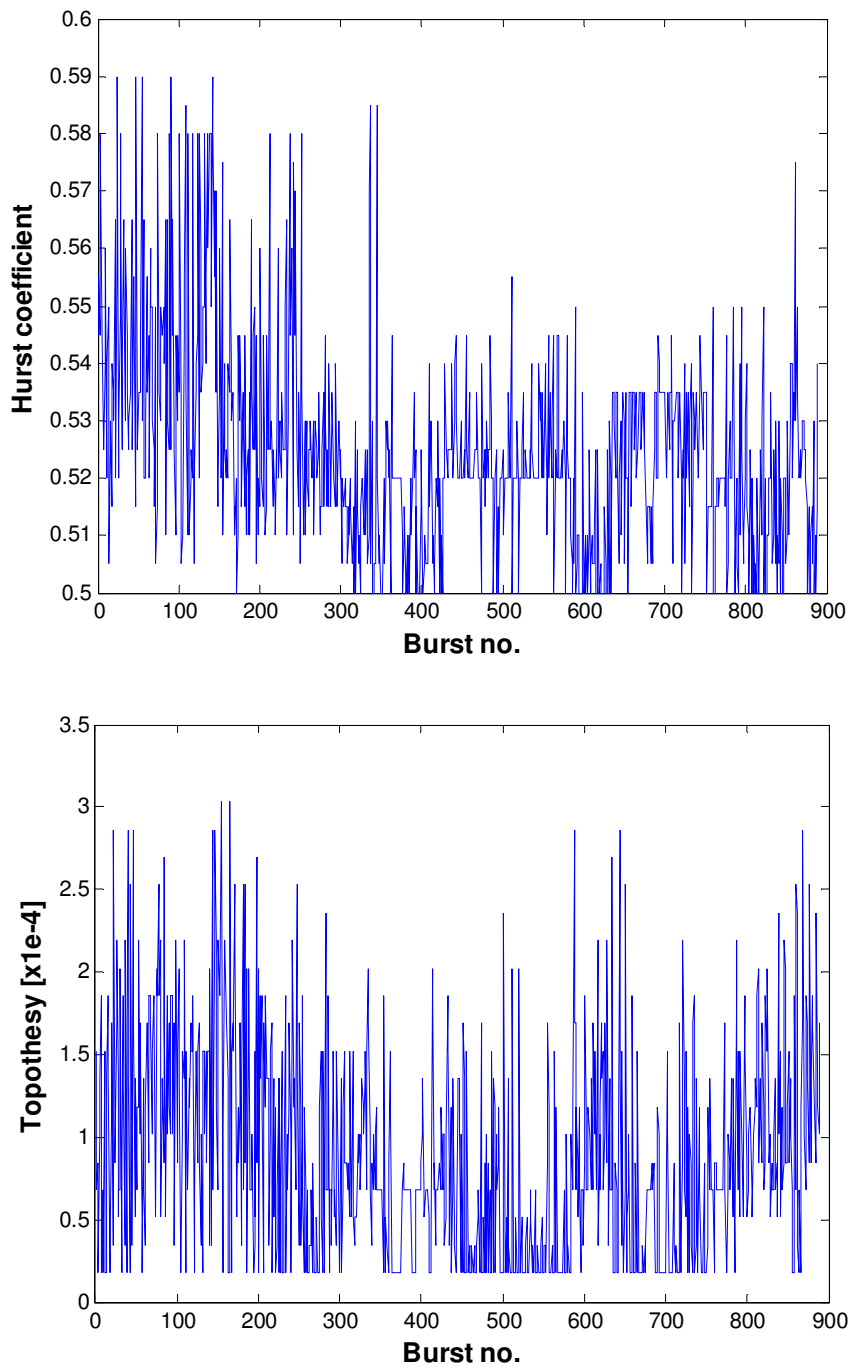


Figure 38 – Final results of the procedure for estimating the fractal parameters applied to T30 fly-by

11 CONCLUSIONS

An analytical model of the average return power waveform, valid for near-nadir altimetry measurements, has been developed in order to cope with the particular operating conditions of Cassini mission. The model is based on the same general assumptions of the classical Brown's model commonly used for oceanographic applications on Earth, but exploits an approximation of the flat surface response by Prony's methods.

The analytical model has been compared with numerically evaluated solutions and it has been found that the mean integral relative error can be kept below 1% by changing the Prony's approximation degree from 2 up to 4 to compensate the increasing off-nadir angle.

This comparison has been also extended either to very low off-nadir angle values, where a closed form of the average return power already exists (nadir model), and to higher values where a different asymptotical approximation based on Laplace's method can be used.

The error analysis allows switching among three different analytical models according to the current off-nadir angle of the measurements, as reported in Table 4.

In addition, in order to infer the significant geophysical parameters describing the surface's topography from the altimetry data, a Maximum Likelihood Estimator (MLE) has been implemented.

This algorithm will be used to process actual data of Cassini mission and to produce standard altimetric Cassini products (Altimeter Burst Data records, ABDR) to be archived in Planetary Data System (PDS) nodes.

The performance of proposed algorithm has been evaluated through simulation and the results are plotted in Figure 11 and Figure 12 for various off-nadir angle and altitude values in the operating range of Cassini radar.

As far as the retrieval of height, the mean value is between ± 6 m almost independently of the used model whereas the standard deviation is about 5 m for nadir model, 15 m for Prony's approximation model and spreads from 10 m up to 25 m for asymptotic model depending on spacecraft altitude.

As far as the retrieval of sigma nought, the mean normalized values is between ± 4 % whereas the standard deviation shows a decreasing behavior for increasing off-nadir angle values starting from about 20 % at nadir up to 4 % at 0.35 degrees.

Further activities have been dedicated to altimetry echo waveform simulation. The main reason for this effort is to better understand the Titan's surface characteristics by analyzing the signals received by CASSINI radar in altimetric mode.

The approach followed is based on a fractal characterization of Titan's surface that enables a closed form for the scattering coefficient.

A preliminary analysis has been performed on actual data (T30 fly-by) for estimating fractal parameters of Titan's surface.

12 APPENDIX A – NADIR MODEL

For a nadir pointing radar altimeter, i.e. off-nadir pointing angle $\xi = 0$, an exact closed-form expression for the flat surface impulse response (FSIR) is available in term of the two-way incremental ranging time, i.e. $\tau = t - 2h/c$, instead of absolute time, under the following general assumptions [7]:

1. the scattering surface may be considered to comprise a sufficiently large number of random independent scattering elements
2. the nature of the scattering mechanism is completely noncoherent
3. the surface height statistics are assumed to be constant over the total area illuminated by the radar during construction of the mean return
4. the specular points are gaussian distributed
5. the scattering is a scalar process with no polarization effects and is frequency independent
6. the variation of the scattering process with angle of incidence (relative to the normal to the mean surface) is only dependent upon the backscattering cross section per unit scattering area, σ^0 , and the antenna pattern
7. the total Doppler frequency spread ($4V_r/\lambda$) due to a radial velocity between the radar and any scattering element on the illuminated surface, is small relative to the frequency spread of the envelope of the transmitted pulse ($2/T$, where T is the 3 dB width of the transmitted pulse)
8. the antenna beam is considered circularly symmetric with gaussian approximation to the antenna gain, i.e., $G(\theta) \approx G_0 \exp(-(2/\gamma) \sin^2 \theta)$
9. for the heights and ranging times of interest $c\tau/h \ll 1$.

Thus, the average backscattered power from a mean flat surface (illuminated by an impulse) which has a very small scale of roughness, but is characterized by the same backscattering cross section per unit scattering area as the true surface, has the following closed form solution for nadir evaluation:

$$P_{FS}(\tau) = K_{FS} \exp(-\alpha\tau) \quad (62)$$

where $K_{FS} = \frac{G_0^2 \lambda^2 c \sigma^0(\psi_0)}{4(4\pi)^2 L_p h^3}$, $\alpha = \frac{4c}{\gamma h}$, $\gamma = -\frac{2 \sin^2(\theta_{3dB}/2)}{\ln(1/2)}$.

Here G_0 is the peak antenna gain (at boresight), c is the speed of light, λ is the radar carrier wavelength, L_p is the two-way path loss, and h is the spacecraft altitude above the mean flat surface.

The geometry of a radar altimeter system, useful for the FSIR evaluation, is given in Figure 39.

We note, according to [7], that the radar cross-section $\sigma^0(\psi, \phi)$ is taken to be ϕ -independent, because of the small pulsewidths and narrow antenna beamwidths. That is, the effective illuminated area covers such a small angular spread that σ^0 may be considered to be nearly constant.

In the following, t_0 is the reference time, i.e. the instant at which the first echo from the surface within the radar footprint is expected to arrive.

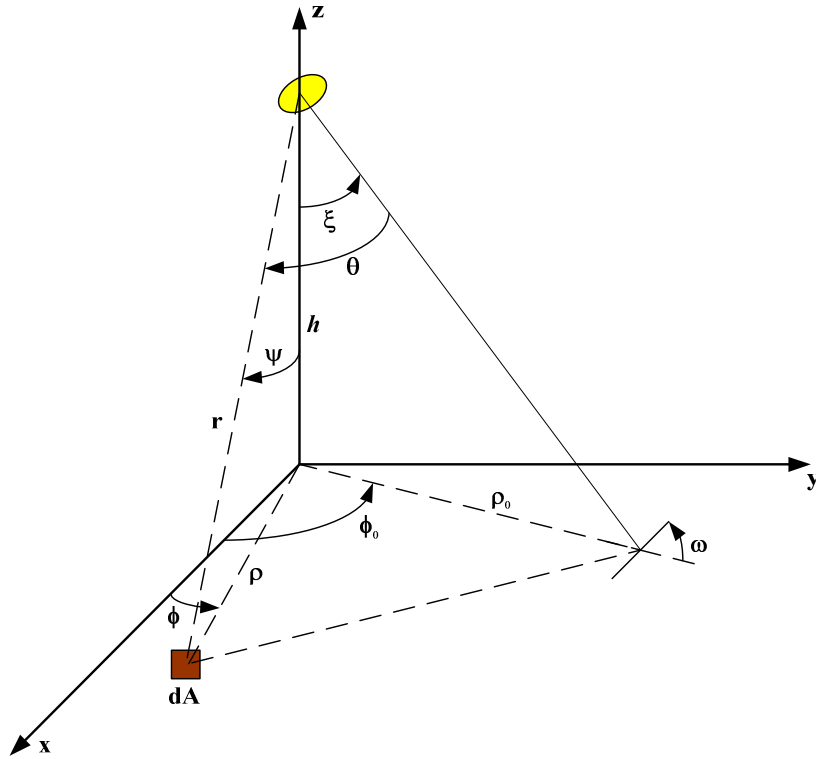


Figure 39 – Geometry for flat-surface impulse response evaluation

The system impulse response can be evaluated, as done in [8], by the convolution of the FSIR with the height probability density function $P_h(\tau)$ and the system point target response $P_p(\tau)$, i.e.,

$$IR(\tau) = P_{FS}(\tau) * P_h(\tau) * P_p(\tau) \quad (63)$$

These two functions are supposed to be Gaussian, and are given by the following expressions:

$$P_h(\tau) = \frac{1}{\sqrt{2\pi}\sigma_h} \frac{c}{2} \exp\left(-\frac{\tau^2 c^2}{2\sigma_h^2 4}\right) \quad (64)$$

$$P_p(\tau) = \frac{P_T T}{\sqrt{2\pi}\sigma_p} \exp\left(-\frac{\tau^2}{2\sigma_p^2}\right) \quad (65)$$

where σ_h is the rms height of the specular points relative to the mean surface level, P_T is the peak transmitted power, and σ_p is related to the 3 dB width of the transmitted pulse by the following relation:

$$\sigma_p = \frac{T}{\sqrt{8 \ln 2}} \quad (66)$$

The convolution between $P_h(\tau)$ and $P_p(\tau)$ can be written as:

$$P_{HI}(\tau) = K_{HI} \exp(-a\tau^2) \quad (67)$$

where $K_{HI} = P_T \eta \sqrt{2\pi} \frac{\sigma_p}{\sigma_c}$, $a = \frac{1}{2\sigma_c^2}$, $\sigma_c^2 = \sigma_s^2 + \sigma_p^2$, $\sigma_s = \frac{2}{c} \sigma_h$, $\eta = BT$.

Here the parameter σ_c is the total spreading of the average echo, which accounts for the surface roughness $\sigma_h 2/c$.

Hence, the system impulse response (20) is given by:

$$\begin{aligned}
P_{FS}(\tau) * P_{HI}(\tau) &= K_{FS} K_{HI} \exp(-\alpha\tau) * \exp(-a\tau^2) = \\
&= K_{FS} K_{HI} \int_0^{\infty} \exp(-\alpha\bar{\tau}) \exp[-a(\tau - \bar{\tau})^2] d\bar{\tau} = \\
&= K_{FS} K_{HI} \exp(-a\tau^2) \int_0^{\infty} \exp(-2b\bar{\tau}) \exp(-a\bar{\tau}^2) d\bar{\tau}
\end{aligned} \tag{68}$$

where $2b = \alpha - 2a\tau$.

By using the Abramowitz and Stegun integration method [4], we have that:

$$\int_0^{\infty} \exp(-2b\bar{\tau}) \exp(-a\bar{\tau}^2) d\bar{\tau} = \frac{1}{2} \sqrt{\frac{\pi}{a}} \exp\left(\frac{b^2}{a}\right) \operatorname{erfc}\left(\frac{b}{\sqrt{a}}\right) \tag{69}$$

which can be substituted in the previous expression to yield:

$$\begin{aligned}
P_{FS}(\tau) * P_{HI}(\tau) &= K_{FS} K_{HI} \frac{1}{2} \sqrt{\frac{\pi}{a}} \exp\left(\frac{b^2}{a}\right) \operatorname{erfc}\left(\frac{b}{\sqrt{a}}\right) = \\
&= K_{FS} K_{HI} \frac{1}{2} \sqrt{\frac{\pi}{a}} \exp\left(\frac{\alpha^2}{4a}\right) \exp(-\alpha\tau) \operatorname{erfc}\left(\frac{b}{\sqrt{a}}\right)
\end{aligned} \tag{70}$$

Now, since $\operatorname{erfc}(\bullet) = 1 - \operatorname{erf}(\bullet)$, the last equation can be written as:

$$\begin{aligned}
P_{FS}(\tau) * P_{HI}(\tau) &= K_{FS} K_{HI} \frac{1}{2} \sqrt{\frac{\pi}{a}} \exp\left(\frac{\delta^2}{2}\right) \cdot \\
&\quad \cdot \exp\left(-\frac{\delta}{\sigma_c} \tau\right) \left[1 + \operatorname{erf}\left(\frac{\tau}{\sqrt{2}\sigma_c} - \frac{\delta}{\sqrt{2}}\right) \right]
\end{aligned} \tag{71}$$

where $\delta = \alpha\sigma_c$. Finally, the system impulse response can be written as reported in following equation:

$$\begin{aligned} IR(\tau)\Big|_{\xi=0} &= P_{FS}(\tau) * P_{HI}(\tau) = \\ &= K\sigma^0 \frac{1}{2} \sqrt{\frac{\pi}{2}} \exp\left(\frac{\delta^2}{2}\right) \exp\left(-\frac{\delta}{\sigma_c} \tau\right) \left[1 + \operatorname{erf}\left(\frac{\tau}{\sqrt{2}\sigma_c} - \frac{\delta}{\sqrt{2}}\right)\right] \end{aligned} \quad (72)$$

where

$$K = \frac{G_0^2 \lambda^2 c}{2(4\pi)^2 L_p h^3} P_T \eta \sigma_p \sqrt{2\pi}.$$

Therefore, the impulse response admits a closed form solution for nadir evaluation. This equation is not dependent of any condition about the altimeter's operative mode, e.g. pulse-limited or not, and it can be considered as a generalization of the Brown's model.

The Brown's approximate expression for the average return power is of the following form:

$$IR(\tau) \approx P_T \eta \sigma_p \sqrt{2\pi} P_{FS}(\tau) \frac{1}{2} \left[1 + \operatorname{erf}\left(\frac{\tau}{\sqrt{2}\sigma_c}\right)\right] \quad (73)$$

which is valid for $\tau \geq 0$. If the altimeter operating conditions vary towards a typical pulse-limited mode, then the equation 72 gives back the classical *Brown echo*, whose validity conditions are met when the parameter δ is small (e.g. $\delta \ll 1$). In fact, in that case, we have that:

$$\frac{\delta^2}{2} \ll \frac{\delta}{\sigma_c} \quad (74)$$

and the term $\delta/\sqrt{2}$ can be neglected with respect to $\tau/\sqrt{2}\sigma_C$.

Since $\delta = \alpha\sigma_C$, in general, the condition $\delta \ll 1$ can be met if:

- 1) $\alpha = f(\gamma^{-1}h^{-1})$ is small, i.e. the spacecraft altitude h increases, given the beamwidth and the pulse duration, and/or the antenna parameter $\gamma = f(\theta_{3dB})$ increases
- 2) σ_C is small, i.e. the parameter σ_p decreases due to a greater bandwidth B .